Check for updates

Received: 24 January 2022 | Revised: 14 November 2022 | Accepted: 15 November 2022 | Published on: 19 December 2022

DOI: 10.1002/qj.4409

Quarterly Journal of the Royal Meteorological Society RMetS

RESEARCH ARTICLE

Flower trade-wind clouds are shallow mesoscale convective systems

Thibaut Dauhut[1] | **Fleur Couvreux**[1] | **Dominique Bouniol**[1] | **Florent Beucher**[1] | **Lea Volkmer**[2] | **Veronika Pörtge**[2] | **Michael Schäfer**[3] | **Alex Ayet**[4,5] | **Pierre-Etienne Brilouet**[1] | **Marek Jacob**[6] | **Martin Wirth**[7]

[1]CNRM, Université de Toulouse, Météo-France, CNRS, Toulouse, France

[2]Meteorologisches Institut, Ludwig-Maximilians-Universität München, Munich, Germany

[3]Leipzig Institute for Meteorology, University of Leipzig, Germany

[4]CNRS, Université Grenoble Alpes, Inria, Grenoble INP, GIPSA-Lab, Grenoble, France

[5]CECI, Université de Toulouse, CNRS, CERFACS, Toulouse, France

[6]Research and Development, Deutscher Wetterdienst (DWD), Offenbach, Germany

[7]Institut für Physik der Atmosphäre, Deutsches Zentrum für Luft- und Raumfahrt, Oberpfaffenhofen, Germany

Correspondence
Thibaut Dauhut, Laboratoire d'Aèrologie (LAERO), Universitè de Toulouse, CNRS, IRD, UT3, 14 avenue Edouard Belin, 31400 Toulouse, France.
Email: thibaut.dauhut@aero.obs-mip.fr

Funding information
Centre National d'Etudes Spatiales; CONSTRAIN EU project; Deutsche Forschungsgemeinschaft, Grant/Award Number: SPP 1294; Max-Planck-Gesellschaft

Abstract

Flower clouds are trade-wind shallow cumuli, with tops reaching 3 km altitude, organised into 100-km wide clusters. They are widespread over the subtropics and associated with the strongest cloud radiative effect among trade-wind cumuli mesoscale organisations. In the context of large uncertainty in climate projections due to the representation of shallow clouds, major knowledge gaps remain about the global impact of mesoscale organisations and the local processes driving them. Here, the processes governing the flower organisation are investigated based on the case study of February 2, 2020 from the Elucidate the Couplings Between Clouds, Convection, and Circulation (EUREC^{4}A) campaign, east of Barbados. One flower cloud is simulated with a large-eddy simulation (LES), using the Meso-NH model at 100-m horizontal grid spacing, and validated extensively with high-resolution observations from the High Altitude and Long-range Research Aircraft (HALO), dropsondes, and satellite measurements. The cloud-top altitudes exhibit a trimodal distribution. The processes shaping flower clouds are wide cold pools and cloudy updrafts organised in one large arc at the western edge. These updrafts are responsible for the highest cloud tops and drive most of the vertical turbulent fluxes of sensible heat, humidity, and momentum. A mesoscale circulation takes place at the scale of the flower clouds and makes them very similar to deep mesoscale convective systems.

KEYWORDS

EUREC^{4}A, flower clouds, LES, mesoscale organisation, shallow convection, trade-wind cumuli

1 | INTRODUCTION

Shallow clouds (with tops lower than 5 km) cover 48% of the global oceans (Eastman *et al.*, 2011), 13% due to cumulus clouds only, and they are associated with large uncertainties in the global radiative budget in both present-day and future climates (Bony and Dufresne, 2005). Their representation in climate models is a source

© 2022 Royal Meteorological Society

of intermodel spread in climate projections. In the trade-wind regions, four mesoscale organisations of shallow clouds were identified in recent years (Stevens *et al.*, 2020) using a combination of subjective identification from a large set of satellite images and machine learning (Rasp *et al.*, 2020). These organisations are named *sugar* when very small clouds cover the ocean uniformly, *gravel* when clouds present arc shapes, *fish* when clouds build fishbone-like networks, and *flower* when clouds are made of 100-km wide clusters (Stevens *et al.*, 2020). Unsupervised automatic organisation identification (Denby, 2020) and metric-based classification (Bony *et al.*, 2020) support the fact that distinct mesoscale shallow cloud organisations are associated with contrasted cloud radiative effects. Among the four named organisations, the flower organisation is very frequent and the most frequent organisation in the east Pacific (up to 50% of the time) a couple of degrees off the coasts of the Americas (Rasp *et al.*, 2020). It is characterized by the strongest cloud radiative effect (about $-15\,\mathrm{W{\cdot}m^{-2}}$), mostly because it has on average the largest low-level cloud fraction among the four organisations (30–50%: Bony *et al.*, 2020). The present study focuses on the flower organisation. The associated wide cloud clusters are called *flower clouds* for the sake of simplicity.

From ground-based radar, flower clouds are characterised by large rain rates and horizontally extended, anvil-like cloud tops at about 3 km altitude (Schulz *et al.*, 2021). Flower clouds are also partly responsible, together with the fish organisation, for most of the cloud fraction above 1.3 km altitude found in the trade-wind region (Schulz *et al.*, 2021). Flower clouds are more frequent than the other mesoscale organisations in large-scale environments characterized by strong surface winds and a strong low-level inversion (about 8–11 $\mathrm{m{\cdot}s^{-1}}$ and 0–4 K estimated inversion strength, the latter being dependent on potential temperatures at 700 hPa and at the surface: Wood and Bretherton, 2006; Bony *et al.*, 2020). In a warming climate, climate models tend to simulate stronger low-level inversions over the tropical western Atlantic (Qu *et al.*, 2015) and uncertain changes in surface wind speed, so the flower organisation might become more frequent (Bony *et al.*, 2020). However, we miss a consistent picture of the processes at mesoscale and finer scales that drive and maintain the flower organisation.

In the frame of the Elucidate the Couplings Between Clouds, Convection and Circulation (EUREC^{4}A) field campaign that took place east of Barbados in January–February 2020 (Bony *et al.*, 2017; Stevens *et al.*, 2021), a wealth of fine-scale observations of shallow clouds were obtained from very diverse platforms, allowing a detailed characterisation of the cloud mesoscale organisation and an investigation of the processes driving them. During the transition from sugar to flower organisations, mesoscale circulations develop and strengthen the heterogeneities in the water-vapour field, making the wet regions (with large vertically integrated water vapour) wetter (Narenpitak *et al.*, 2021), consistent with the gross moist instability that drives shallow cloud clustering over the Pacific ocean (Bretherton and Blossey, 2017). Increased large-scale upward vertical velocities (of the order of $2\,\mathrm{cm{\cdot}s^{-1}}$ instead of $1\,\mathrm{cm{\cdot}s^{-1}}$, up to about 4 km altitude in this region, where subsiding motions dominate above) tend to foster such a mechanism and the development of flower clouds in wet regions. The role played by submesoscale processes (especially at scales finer than about 2 km) in mesoscale cloud organisation remains unclear, however. In particular, the circulations in the subcloud layer were found to be crucial for the organisation of shallow clouds, ever since pioneering observational studies, including LeMone and Pennell (1976), first associated subcloud circulations with clouds over the ocean directly. Among them, Zuidema *et al.* (2012) reported observations of cold pools, i.e., dense air masses that sink and spread at the surface. These cold pools have been observed to damp cumulus formation over large areas, organising the cumulus field. For the specific case of February 2, 2020 observed during EUREC^{4}A, several cold pools were observed in the vicinity of flower clouds (Touzé-Peiffer *et al.*, 2022), but their role in the organisation of clouds needs to be elucidated.

To investigate the convective processes at play, the numerical modelling approach is convenient, as it provides comprehensive and consistent 4D fields of dynamical and thermodynamical variables. Cloud-resolving simulations using kilometric horizontal grid spacing can represent the mesoscale organisation and its day-to-day variability successfully (Beucher *et al.*, 2022). However, they employ a parametrisation of shallow convection and therefore do not resolve the cumulus explicitly, impeding investigation of the fine-scale circulations at play. In this study we use a large-eddy simulation (LES, with a grid spacing of 100 m) forced by a cloud-resolving simulation to represent these circulations explicitly over a $200 \times 100\,\mathrm{km}^2$ domain. The combination of such a simulation with high-resolution observations from spaceborne and airborne instruments allows us to characterise flower-cloud organisation and investigate the driving processes at play in the subcloud and cloud layers.

The article is structured as follows. Section 2 describes the meteorological conditions of the case study on February 2, 2020, characterised by clear flower organisation of the clouds, and High Altitude and Long-range Research Aircraft (HALO) aircraft observations in the frame of the EUREC^{4}A field campaign, complementary satellite observations, and the model configuration used to perform the LES. Section 3 presents a characterisation of flower clouds

1477870x, 2023, 750, Downloaded from https://rmets.onlinelibrary.wiley.com/doi/10.1002/qj.4409 by Portail BibCNRS INSU, Wiley Online Library on [25/10/2023]. See the Terms and Conditions (https://onlinelibrary.wiley.com/terms-and-conditions) on Wiley Online Library for rules of use; OA articles are governed by the applicable Creative Commons License

1477870x, 2023, 750, Downloaded from https://rmets.onlinelibrary.wiley.com/doi/10.1002/qj.4409 by Portail BibCNRS INSU, Wiley Online Library on [25/10/2023]. See the Terms and Conditions (https://onlinelibrary.wiley.com/terms-and-conditions) on Wiley Online Library for rules of use; OA articles are governed by the applicable Creative Commons License

and their environment, based on both the observations and the LES. Section 4 investigates the convective processes at play in flower clouds, leveraging the LES 4D fields. In particular, updrafts and cold pools are identified and their contribution to the vertical turbulent fluxes is computed. Section 5 is a discussion that puts the results from Sections 3 and 4 in perspective, highlighting specific questions that remain to be investigated. Section 6 summarises the conclusions of the analysis.

2 | CASE STUDY, HIGH-RESOLUTION OBSERVATIONS AND MODEL

2.1 | Synoptic environment of the case study on February 2, 2020

East of Barbados, in the region of intensive measurements by the EUREC^{4}A field campaign, February 2, 2020 is characterized by mild zonal wind (5 m·s^{-1} at 10 m altitude), relatively low vertically integrated water vapour, hereafter called precipitable water (PW, lower than 30 kg·m^{-2}), and significantly large low-level stability (estimated inversion strength larger than 7 K, whereas values are lower than 4 K during the rest of the campaign). This date is selected for our case study, as the trade-wind cumuli adopted a clear flower organisation. The flower clouds were about 100 km wide and ubiquitous over the region of investigation (Figure 1). In contrast to flower organisations on later days, the trade winds were not as strong: the zonal wind became steadily larger than 7 m·s^{-1} from February 5 onwards, leading to fast advection of the flower clouds. The latter situation is more difficult to simulate with a LES on a fixed domain, as the flower clouds would rapidly be advected out of the domain. February 2 was selected as a convenient date, with a cloud residence time of about 7 hr in the 200-km large domain of the LES. Even if a mild zonal wind at 10 m altitude is unusual for flower clouds (Bony *et al.*, 2020), the February 2 zonal wind was much stronger at higher altitude (9–10 m·s^{-1} at 3 km: Beucher *et al.*, 2022).

2.2 | HALO aircraft measurements

During EUREC^{4}A, HALO was deployed east of Barbados (Konow *et al.*, 2021; Stevens *et al.*, 2021). Each flight was planned with a circle track designed to capture the mesoscale variability of the atmosphere and to measure the mesoscale vertical velocity (Bony and Stevens, 2019). Throughout February 2, the HALO aircraft was flying the same circle pattern six times and during the afternoon there was a "clover pattern" (made of three leaves) through the circle region (Figure 1b). From HALO, a set of active and passive remote-sensing instruments was operated and dropsondes were launched each 2–8 minutes during each circle, which took one hour to complete. The in situ measurements from the dropsondes are gathered and regridded in the Joint dropsonde Observations of the Atmosphere in tropical North atlaNtic mesoscale Environments (JOANNE) dataset (George *et al.*, 2021). From the active remote sensors, the water-vapour differential absorption measurements from the WAter vapor Lidar Experiment in Space (WALES: Wirth *et al.*, 2009) are used to characterise the water-vapour structure in the cloud-free atmosphere, while the cloud masks from WALES and the HALO Microwave Package (HAMP) radar (Mech *et al.*, 2014) are used to retrieve the cloud-top altitudes (Table 1). From the passive remote sensors, the HAMP radiometers measured the vertically integrated water-vapour and liquid water path (Jacob *et al.*, 2019). Two-dimensional cloud masks from the Video airbornE Longwave Observations with siX channels (VELOX: Schäfer *et al.*, 2021) and the shortwave infrared spectrometer of the Munich Aerosol Cloud Scanner (specMACS: Ewald *et al.*, 2016) provide estimates of the cloud fraction with an uncertainty range. In addition, cloud-top heights are retrieved from measurements of the (polarization-resolving) RGB camera of specMACS using a stereographic reconstruction method (Kölling *et al.*, 2019). VELOX is a thermal infrared camera system which measures the brightness temperature of the upward radiance field. Four different brightness temperature thresholds are used to create a cloud mask. The specMACS cloud mask is based on the radiance measurements of the short-wave infrared camera of the system and identifies cloudy pixels by their brightness and the measured water-vapour absorption. The characteristics of the observational products, and their sampling resolution in particular, are detailed in Table 1. An additional description of the HALO flight and technical characteristics of the instruments can be found in Konow *et al.* (2021). Combining as many HALO measurements as possible, together with the satellite measurements described hereafter, leverages each instrument's strengths and weaknesses and provides a spread in the estimates of the investigated parameters.

2.3 | Satellite measurements

Cloud cover and cloud-top altitude in the LES are assessed using visible reflectance and infrared brightness temperature measurements from the Advanced Baseline Imager on board the geostationary satellite *GOES-16*. Channels 2 and 13 at 0.64 and 10.35 μm, respectively, were used. The horizontal resolutions of the reflectance and brightness

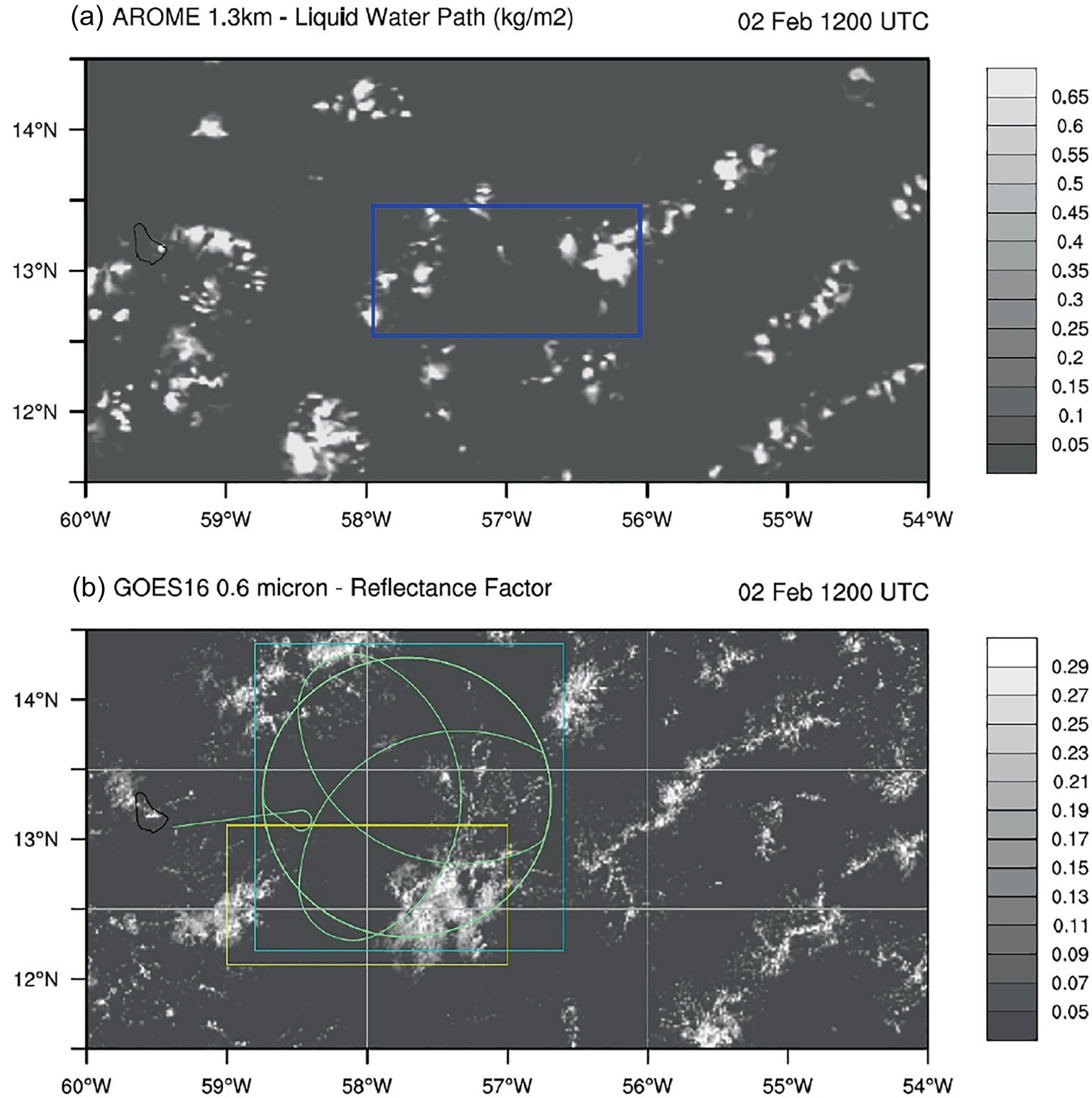

FIGURE 1 Domain of investigation in the tropical Atlantic, east of Barbados island: (a) liquid water path from AROME-OM model forecast, used to initialise the Meso-NH model, and (b) reflectance factor (unitless) in the 0.6-μm channel of *GOES-16* geostationary satellite observations, both at 1200 UTC on February 2, 2020. In (a), the Meso-NH domain used for the LES is delimited in blue. In (b), the HALO aircraft flight track is in green, the control domain used to compare *GOES* imagery with Meso-NH LES is in yellow, the square domain is in cyan, and the paving domains are in grey [Colour figure can be viewed at wileyonlinelibrary.com]

temperature are 500 m and 2 km, respectively. For the evolution of the cloud cover, the infrared brightness temperature measurements are available every 10 min. The measurements are sampled over three different types of subdomain, described hereafter. The *control domain* (yellow in Figure 1b) has the same dimensions as the LES domain, but is located slightly more southwest. Its location is chosen in order to guarantee that the evolution of the flower cloud at 12–12.5°N is captured well in satellite observations. The *nine paving domains* (grey in Figure 1b) have the same dimensions as the control domain and pave the area as shown in Figure 1b. The *square domain* from 12.2–14.4°N and from −58.8 to −56.6 °E (cyan in Figure 1b) encompasses the HALO circle fully.

To validate the low-level circulation in the LES qualitatively, the horizontal variability of the surface wind-speed anomalies is compared with *Sentinel* low-Earth-orbiting satellite Synthetic-Aperture Radar (SAR) measurements of sea-surface roughness, on days exhibiting flower organisation of the trade-wind clouds. SAR backscatter captures the footprints of atmospheric processes close to the sea surface, such as small-scale turbulence (Young *et al.*, 2000) and cold-pool-induced winds (Atlas *et al.*, 1995). It shows good agreement with LES winds (Ayet *et al.*, 2021) and in situ

1477870x, 2023, 750, Downloaded from https://rmets.onlinelibrary.wiley.com/doi/10.1002/qj.4409 by Portail BibCNRS INS2I, Wiley Online Library on [25/10/2023]. See the Terms and Conditions (https://onlinelibrary.wiley.com/terms-and-conditions) on Wiley Online Library for rules of use; OA articles are governed by the applicable Creative Commons License

TABLE 1 Characteristics of observational products from the HALO flight on February 2, 2020. The swath is given as the observed section of sea surface across-track for a flight altitude of 10 km. dx, dz, and dt stand for horizontal, vertical, and temporal resolution, respectively. CM stands for cloud mask. BT, T, p, q_v, r_v, PW, and LWP stand for brightness temperature, temperature, air pressure, specific humidity, water-vapour mixing ratio, precipitable water, i.e., vertically integrated water-vapour mass, and liquid water path, i.e., vertically integrated cloud liquid water mass, respectively

Variable	Product	Swath	dx	dz	dt
Cloud fraction	specMACS SWIR CM	6.4 km	20 m	N/A	0.1 s
Cloud fraction	VELOX CM	6.4 km	9 m	N/A	1 s
Cloud-top altitude	specMACS POL-RGB CTH	30 km	10–30 m	N/A	0.05–0.15 s
Cloud-top altitude	WALES CM	1 point	40 m	7.5 m	0.2 s
Cloud-top altitude	HAMP radar CM	1 point	200 m	30 m	1 s
Cloud-top BT	VELOX BT 7.7–12 μm	6.4 km	9 m	N/A	1 s
PW	HAMP radiometer PW	1 point	200 m	N/A	1 s
LWP	HAMP radiometer LWP	1 point	200 m	N/A	1 s
T, p, and q_v	JOANNE dropsonde in situ	1 point	N/A	10 m	N/A
r_v	WALES water vapour	1 point	2.4 km	15 m	12 s

measurements (Brilouet *et al.*, 2022). Since no large-swath SAR measurements were available in the study region on February 2, 2020, two other dates with flower organisation of the trade-wind cumuli, namely February 8 and 13, 2020, were selected.

2.4 | Meso-NH model and LES setup

The flower-cloud development and propagation on February 2, 2020 is simulated with the anelastic nonhydrostatic mesoscale model Meso-NH (Lac *et al.*, 2018). The domain of 204.8 km × 102.4 km spans the region [12.5, 13.5]°N, [−57.9, −56.1]°E (Figure 1a) in the tropical Atlantic, just east of Barbados, where intensive measurements were performed during the EUREC^{4}A field campaign. The domain is large enough to simulate one flower cloud. The horizontal grid spacing is 100 m in order to resolve the larger thermals of the subcloud layer and the larger cloud eddies. The vertical grid spacing is uniformly equal to 40 m to sample layers of strong vertical gradient finely at the surface, subcloud-layer top, and trade-wind inversion. The model top is at 5,200 m altitude, with a sponge layer from 4,000 m altitude upward to prevent reflection of gravity waves. The model was initialised at 1200 UTC on February 2, 2020 and ran for 7 hr. The time step is 1 s. The initial and lateral boundary conditions come from the AROME-OM forecast on February 2, 2020 that ran with a horizontal grid spacing of 1.3 km (Beucher *et al.*, 2022). The Meso-NH atmosphere is initialised with the AROME-OM fields after 12 hr of integration of AROME-OM, interpolated on the LES grid. The values of the meteorological fields (wind, temperature, pressure, water mixing ratios) along the lateral boundaries are updated every hour from AROME-OM fields, with temporal interpolation between the updates. A one-hour frequency for the updates is chosen in order to sample the diurnal variations of the large-scale environment. No large-scale tendency is imposed in the Meso-NH domain.

Shallow convection is represented explicitly without the use of any convective parametrisation. Clouds, precipitation, and microphysical processes are represented with a one-moment microphysical scheme (Pinty and Jabouille, 1998) that uses five prognostic mass mixing ratios for the hydrometeors: rain, cloud liquid water, snow, graupel, and cloud ice. Only rain and cloud liquid water are nonzero in the LES, since the atmosphere is simulated above freezing temperature everywhere in the domain. Most of the turbulent structures are resolved by the model; however, a 3D turbulence scheme based on a 1.5-order closure (Cuxart *et al.*, 2000) is used to represent small-scale turbulence. The radiative heating and cooling rates are calculated every minute with the radiative scheme used at the European Centre for Medium-Range Weather Forecasts (Gregory *et al.*, 2000).

3 | CHARACTERISATION OF FLOWER CLOUDS AND THEIR ENVIRONMENT

This section has two objectives: first to validate the LES in detail with respect to the available observations, and second to characterise flower clouds and the surrounding

1477870x, 2023, 750, Downloaded from https://rmets.onlinelibrary.wiley.com/doi/10.1002/qj.4409 by Portail BibCNRS INSU, Wiley Online Library on [25/10/2023]. See the Terms and Conditions (https://onlinelibrary.wiley.com/terms-and-conditions) on Wiley Online Library for rules of use; OA articles are governed by the applicable Creative Commons License

clear sky, combining high-resolution observations and the LES. To discuss the macroscopic properties of the cloud and the structure of the surface winds, two times are selected to represent two contrasting shapes of the flower cloud: 1300 UTC in its early stage and 1600 UTC when it is well developed. These two times capture the small variability in shape seen at other times.

3.1 | Bulk cloud properties

Two bulk cloud properties are compared with observations in order to evaluate the cloud formation in the LES: the cloud fraction (Figure 2) and the frequency distribution of cloud-top altitudes (Figures 3 and 4). Evolution of the cloud fraction during the seven hours of simulations is compared with the measured one using specMACS and VELOX on board HALO, averaged every hour, and the value deduced from *GOES-IR* imagery using a 293-K threshold (Figure 2). The value of 293 K is selected as the closest isotherm level to the lifting condensation level . This level has been estimated from all HALO dropsondes during the campaign (not shown). From the LES, the cloud fraction is computed at a 1-hr frequency. From the HALO cameras, averaging over 1 hr leads us to consider an area that is 220 km wide (the HALO circle diameter), similar to the LES domain. Cloud fractions deduced from *GOES-IR* are computed every 10 min, which is the highest frequency available.

In the LES, the cloud fraction has a slow evolution (Figure 2) from about 22% at 1300 UTC to 34% at 1700 UTC, and then starts to decrease as the simulated flower cloud is advected out of the domain by the trade winds. To estimate the uncertainty in the simulated cloud fraction, two thresholds are used to detect the clouds in the simulation: 10^{-5} and 10^{-6} kg·kg^{-1}. SpecMACS and VELOX measured cloud fractions very similar in both amplitude and variation. The drop in observed cloud fraction is earlier, however, due to the fact that the HALO aircraft sampled fewer clouds from 1700 UTC onward. The uncertainty range is much larger for VELOX than for specMACS, because more pixels are associated with the "probably cloudy" class in the VELOX cloud mask than in the specMACS one. The cloud fraction estimated from *GOES-IR* imagery over both the control domain and the fixed square domain also matches the simulated evolution and the one observed by HALO cameras well. However, as highlighted by the cloud fraction from the nine paving domains, the cloud fraction is very sensitive to whether a flower cloud is passing in the domain or not. Over the nine paving domains, the cloud fraction can range from 2 to 40%, for example, at 1900 UTC. This underlines the strong modulation that flower clouds produce on the cloud fraction at the mesoscale, over areas as large as one grid cell of a climate model.

The cloud shape is investigated based on two snapshots of the cloud distribution, at 1300 and 1600 UTC, from *GOES* visible, *GOES-IR*, and LES in Figure 3. All exhibit a typical round shape. At 1600 UTC, a small flower cloud is visible in the eastern parts of the control and LES domains. In Figure 3b, the lowest values of brightness temperature, associated with the highest cloud tops, are organised in an arc in the western part of the flower cloud. This is also visible in the simulated flower cloud at 1600 UTC (Figure 3f). This arc shape is confirmed by the *GOES* visible imagery (Figure 3a); note, however, that the reflectance factor measured by the visible channel is not linked to the cloud-top altitude but rather to the liquid water path.

The observed and simulated cloud-top altitude distributions are compared in Figure 4, and overlaid with the

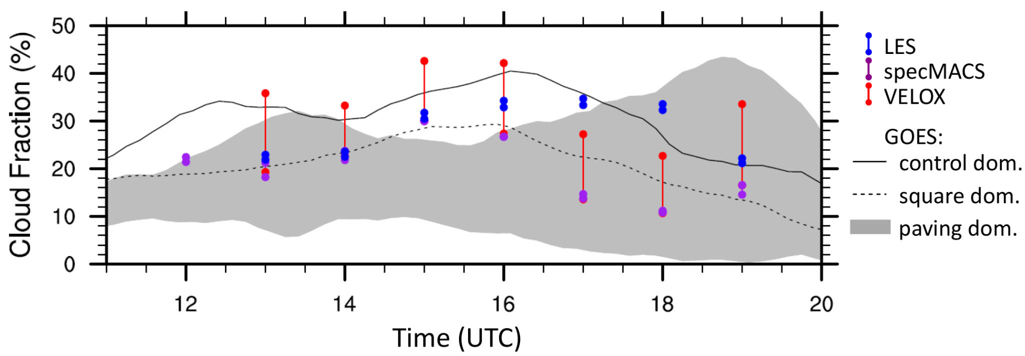

FIGURE 2 Evolution of the cloud fraction in the LES (blue), HALO measurements (specMACS (purple), VELOX (red)), and *GOES* imagery from the infrared 10.35-μm channel: over the control domain (solid line), nine domains paving the region of Figure 1 (grey shading), and square domain covering the whole HALO circle (dotted line). The vertical lines illustrate the uncertainty ranges computed using two different thresholds to detect the clouds in the LES and using the maximal and minimal cloud fraction estimates in specMACS and VELOX cloud-mask products [Colour figure can be viewed at wileyonlinelibrary.com]

1477870x, 2023, 750, Downloaded from https://rmets.onlinelibrary.wiley.com/doi/10.1002/qj.4409 by Portail BibCNRS INSU, Wiley Online Library on [25/10/2023]. See the Terms and Conditions (https://onlinelibrary.wiley.com/terms-and-conditions) on Wiley Online Library for rules of use; OA articles are governed by the applicable Creative Commons License

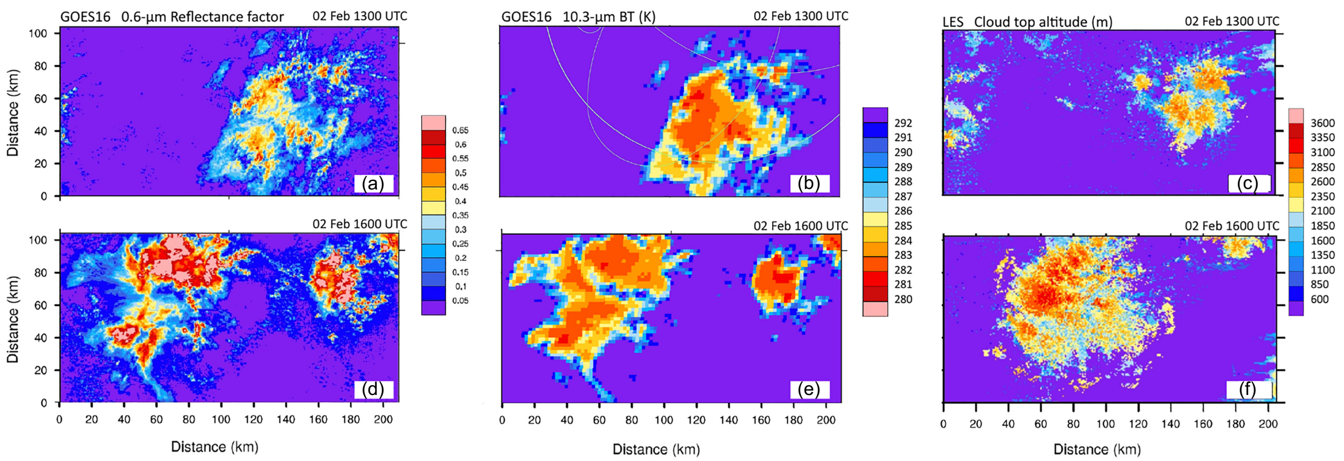

FIGURE 3 Maps at (a–c) 1300 UTC and (d–f) 1600 UTC of (a,d) reflectance factor from *GOES* 0.6-μm visible channel, (b,e) BT (brightness temperature) from *GOES* 10.35-μm infrared channel, and (c,f) cloud-top altitude from Meso-NH LES [Colour figure can be viewed at wileyonlinelibrary.com]

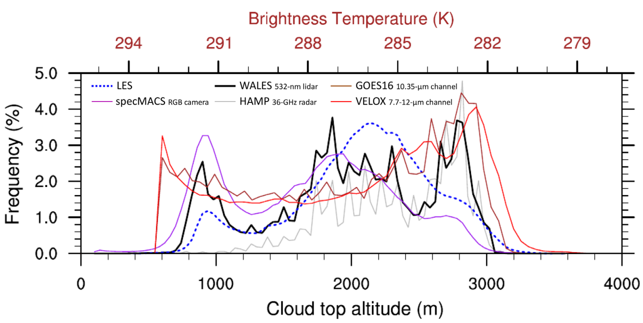

FIGURE 4 Cloud-top distribution in terms of altitudes using uniform 40-m bins: LES (blue), specMACS RGB camera (purple), WALES lidar (thick black), and HAMP cloud radar (grey); and in terms of BT using uniform 0.25-K bins: *GOES* 10.35-μm infrared channel (brown) and VELOX 7.7-12-μm infrared channel (red). For LES, hourly outputs are used from 1300–1900 UTC. For specMACS, WALES, HAMP cloud radar, and VELOX, the whole measurements on February 2, 2020 are used. For *GOES*, the measurements every hour from 1200–1900 UTC are used [Colour figure can be viewed at wileyonlinelibrary.com]

observed cloud-top brightness temperature (BT) distributions (with 0.25-K bins). To overlay these distributions, we assumed that the 292- and 282-K BTs correspond to cloud tops at 800- and 3,000 m altitudes, respectively, based on clear-sky and high-cloud in situ profiles of temperature (see later: Figure 6e,h). The cloud-top altitudes exhibit a clear trimodal distribution both in lidar and visible camera observations and in LES. The highest mode, slightly below 3 km altitude, is, however, much less pronounced in the LES and specMACS than in the lidar observations (an explanation for specMACS is given in the Supporting Information). The amplitude of the second mode, at about 2 km altitude, is more important in the LES than in the lidar observations, both absolutely and relative to the two other modes. The distribution from the radar observations is similar to the one from lidar observations, except that it misses the first mode slightly below 1 km altitude. This is expected, assuming that this mode is made of smaller and thinner clouds, with smaller droplets, more difficult to sample by the radar signal than the other two modes. The brightness temperature distributions from VELOX and *GOES-IR* are very consistent with each other. Mostly two modes can be seen in the VELOX distribution, at 293 and 282 K; an intermediate one at 284 K is barely noticeable. In *GOES-IR*, large fluctuations of frequency with BT (due to limited spatial resolution) prevent the identification of any intermediate mode: only two are visible at 293 and 283 K.

This first assessment of the cloud properties highlights that the LES produces a flower cloud in line with the observed ones, in terms of both shape and area. This flower cloud is simulated throughout the simulation, consistent with the observed flower clouds, which last at least 7 hr. Details of the cloud-top distribution are also consistent between the LES and the observations: the highest clouds are organised in an arc, and three modes are found in the cloud-top altitude distribution, at about 1, 2, and 3 km altitudes. The relative importance of the different modes is, however, different in the LES compared with the observations: the simulated first and third modes are less frequent in the LES than in the observations. Investigations of the cloud-top altitudes where HALO overpassed the targeted flower cloud, detailed below, indicate that the weaker third mode in the LES is due to narrower cloud tops reaching 3 km altitude compared with the observations.

1477870x, 2023, 750, Downloaded from https://rmets.onlinelibrary.wiley.com/doi/10.1002/qj.4409 by Portail BibCNRS INSU, Wiley Online Library on [25/10/2023]. See the Terms and Conditions (https://onlinelibrary.wiley.com/terms-and-conditions) on Wiley Online Library for rules of use; OA articles are governed by the applicable Creative Commons License

3.2 | Full-sky thermodynamical properties

The thermodynamical properties of the simulated atmosphere are compared with HAMP radiometer measurements from HALO (Figure 5) and in situ measurements collected from dropsondes and compiled in the JOANNE dataset (Figure 6). The HAMP radiometer measures precipitable water (PW) and liquid water paths (LWP), while the JOANNE dataset describes the vertical structure of the atmosphere.

The PW distribution over the full period of simulation and the HALO flight is monomodal and positively skewed in both the simulation and the HAMP radiometer measurements (Figure 5a). The most frequent values are 27 and 30 $kg{\cdot}m^{-2}$ in the LES and observations, respectively. The LES tends to overestimate the frequencies of the lowest and largest values compared with the HAMP radiometer. In line with this, the LES presents lower average PW but larger standard deviation than the observations (30.8± 4.4 $kg{\cdot}m^{-2}$ versus 31.0± 3.6 $kg{\cdot}m^{-2}$), consistent with the forcing model AROME-OM (figure 11a in Beucher *et al.*, 2022). The distribution of LWP shows a clear maximum at low values and a steady decrease towards larger values. The LES represents the slope of the decrease well, but its average LWP is larger than that of observations (0.40 versus 0.33 $kg{\cdot}m^{-2}$) and it tends to overestimate the frequency of nonzero LWP values systematically. The latter might be due to the fact that the HAMP radiometer sampled few flower clouds in the late afternoon, when the HALO aircraft flew in between these clouds. This is consistent with the cloud fraction observed by HALO instruments that drops earlier than the LES cloud fraction (Figure 2).

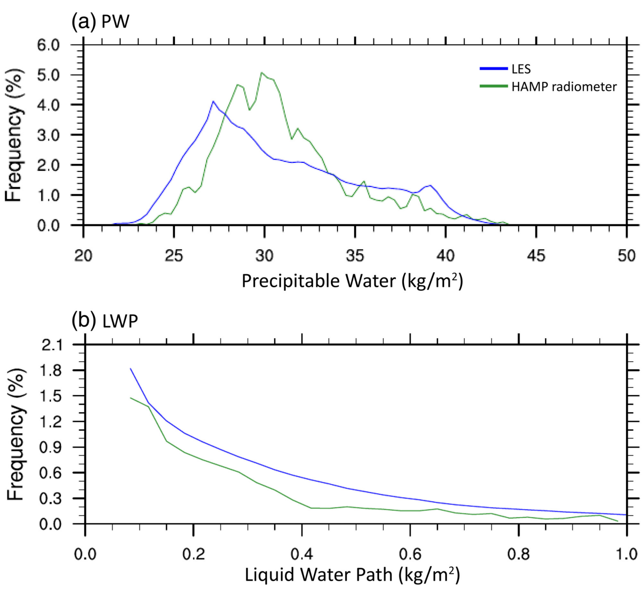

FIGURE 5 Distribution of vertically integrated (a) water vapour PW, and (b) cloud liquid water LWP, from HAMP radiometer over the whole HALO flight in green and LES output every hour in blue. Average (standard deviation) of PW is 31.0 (3.6) $kg{\cdot}m^{-2}$ in the HAMP radiometer measurements versus 30.8 (4.4) $kg{\cdot}m^{-2}$ in the LES, and for LWP 0.33 (0.27) $kg{\cdot}m^{-2}$ in the HAMP radiometer measurements versus 0.40 (0.35) $kg{\cdot}m^{-2}$ in the LES [Colour figure can be viewed at wileyonlinelibrary.com]

The vertical thermodynamical structure of the simulated atmosphere is assessed using the JOANNE dropsonde in situ measurements of water vapour and air temperature, presented as specific humidity and potential temperature (Figure 6). WALES vertical profiles of specific humidity above cloud top are shown in addition in Figure 6a–d. To capture the variability of the profiles, the atmospheric columns are subdivided into four categories, matching the observed and simulated three modes in cloud-top altitude distribution (cf. Figure 4): clear sky, shallowest clouds, middle clouds, and highest clouds, depending on whether the cloud tops are absent, between 0.6 and 1.3 km, between 1.3 and 2.5 km, or above 2.5 km, respectively. Cloud tops are detected at the highest level where the cloud liquid water mixing ratio drops below 10^{-6} $kg{\cdot}kg^{-1}$ in the LES, where the relative humidity drops below 95% in the dropsondes profile, and using the nearest cloud-top detection from the WALES cloud mask for the WALES profiles. For both specific humidity and potential temperature, the range of values is larger in the LES than in the dropsondes (and in WALES measurements), because the dropsondes (and WALES profiles to a lesser extent) are much fewer than the columns in the LES for all categories (see Figure 6).

The vertical structure of the specific humidity field shows that the LES is in excellent agreement with the dropsondes up to 600, 1,200, and 1,800 m for clear sky, the shallowest clouds, and the middle clouds, respectively. Above, the LES tends to be too moist, underestimating the dryness of the overlying dry layers. The clear-sky profiles suggest that the LES subcloud layer is slightly too deep (about 100 m) compared with the observations. This is consistent with the clear-sky potential temperature profile (Figure 6e). This bias is probably inherited from the forcing model (Beucher *et al.*, 2022). For the highest clouds, the LES tends to be too moist throughout the average profile, up to 2,300 m. This might be due to the fact that comparison of dropsonde profiles with LES column profiles assumes implicitly that the dropsondes fall vertically. A small horizontal displacement in the dropsonde trajectory might lead to differences in the comparison, especially in highest-cloud columns where updrafts are frequent (cf. later: Figure 11d). The WALES average specific humidity profiles align with JOANNE ones in clear sky, but tend to be much drier than JOANNE profiles above the

1477870x, 2023, 750, Downloaded from https://rmets.onlinelibrary.wiley.com/doi/10.1002/qj.4409 by Portail BibCNRS INS2I, Wiley Online Library on [25/10/2023]. See the Terms and Conditions (https://onlinelibrary.wiley.com/terms-and-conditions) on Wiley Online Library for rules of use; OA articles are governed by the applicable Creative Commons License

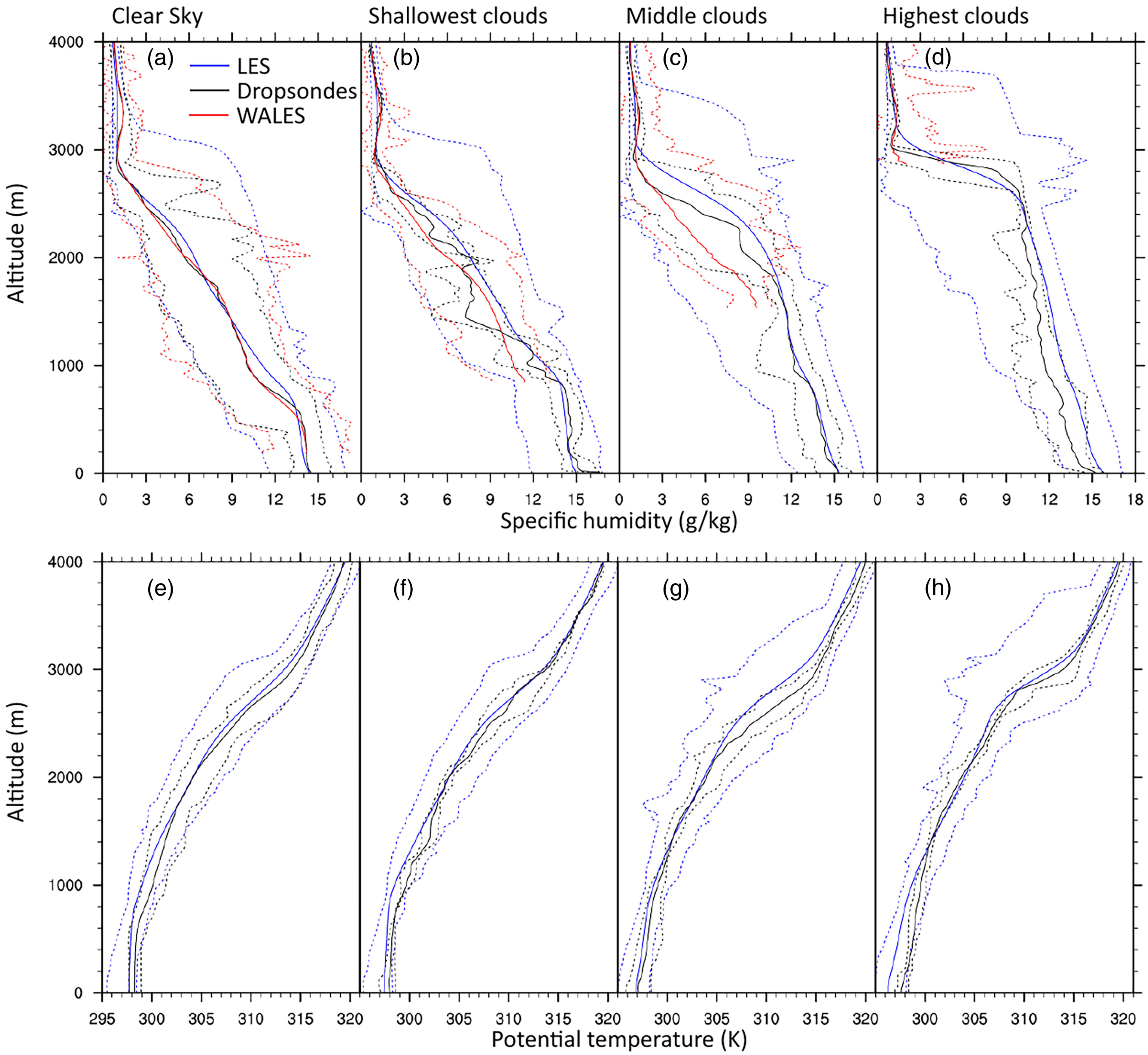

FIGURE 6 Vertical profiles of (a–d) specific humidity and (e–h) potential temperature, from LES (using output every hour between 1300 and 1800 UTC) in blue, JOANNE dropsonde in situ measurements in black, and WALES water-vapour profiles above cloud top in red (using all measurements on February 2, 2020 for the latter two). The average profile is shown by a solid line and the minimum and maximum as dashed lines. Profiles are sorted depending on the altitude of the cloud tops: (a,e) clear-sky (58 dropsondes, 8.8×10^6 columns in the LES, 1,653 profiles in WALES), (b,f) shallowest clouds with tops below 1.3 km (three dropsondes, 0.4×10^6 columns in the LES, 110 profiles in WALES), (c,g) intermediate clouds with tops between 1.3 and 2.5 km (eight dropsondes, 2.6×10^6 columns in the LES, 360 profiles in WALES), and (d,h) deepest clouds with tops above 2.5 km (seven dropsondes, 0.8×10^6 columns in the LES, 174 profiles in WALES). For WALES in (a–d), the values are shown at all altitudes where at least 10 profiles have nonmissing values [Colour figure can be viewed at wileyonlinelibrary.com]

middle clouds (Figure 6c). This difference might be due to the reduced number of dropsondes in that category. In terms of potential temperature, the LES average profile is in very good agreement for middle clouds, up to 2,200 m, but it is up to 2.5 K too cold above this. For clear sky, the shallowest clouds, and the highest clouds, the LES tends to be too cold, up to 1 K colder than in situ observations. From both specific humidity and potential temperature, it appears that the transition from cloud top to the cloud-free troposphere above is less sharp in the LES than in the dropsonde observations. This might be due to more intense mixing at the cloud tops (consistent with the large range of values in the LES), but also the larger number of profiles from the LES than from the dropsonde

1477870x, 2023, 750, Downloaded from https://rmets.onlinelibrary.wiley.com/doi/10.1002/qj.4409 by Portail BibCNRS INSU, Wiley Online Library on [25/10/2023]. See the Terms and Conditions (https://onlinelibrary.wiley.com/terms-and-conditions) on Wiley Online Library for rules of use; OA articles are governed by the applicable Creative Commons License

dataset. The latter interpretation seems to be confirmed, given the smooth transition in WALES profiles, which are also significantly more numerous than dropsonde profiles. The LES variability is also much larger near the trade-wind inversion (2.5–3 km altitude) than in the dropsonde profiles. This may be due to overshooting clouds, which are easily missed in these observations.

3.3 | Zooming in on HALO flower-cloud overflights

The microscale structure of flower clouds and their close environment is further assessed considering the heterogeneity of cloud-top temperatures (Figure 7) and the stratification of humidity around clouds (Figure 8). For both, seven overpasses of the HALO aircraft above the southern flower cloud (in the control domain of Figure 1b) are selected and analysed.

The LES cloud-top temperature distribution is compared with VELOX broad-band brightness temperature measurements between 7.7 and 12 µm in two dimensions: the across-track dimension of the sensor and the time dimension; in other words, a two-dimensional pushbroom image was compiled from all measurements of the centre swath line along the flight track. The WALES measurements, which show the best skill to capture the trimodal distribution of cloud tops (Figure 4), are not used here because of the narrow swath (Table 1). During the day, from the first to the seventh HALO overpass, the VELOX measurements (Figure 7: left column and red line in the right column) indicate cloud-top cooling, reproduced in the LES (Figure 7: central column and blue line in the right column). The cloud-top temperature distribution looks smoother in the VELOX measurements than in the LES, however. This is confirmed by the cloud-top (brightness) temperature frequency distributions: three modes appear most of the time in the LES, whereas these modes seem smoothed down to a monomodal distribution in the observations, especially in the late afternoon. This might be because the LES struggles to represent an anvil or veil spread, or because the sensitivity of the IR brightness temperature sensors is too low to sample the trimodal distribution (see the comparison of cloud-top distributions in Figure 4). In line with this later point, the coldest cloud tops are more frequent in the LES than in the VELOX measurements. Concerning the second mode, the VELOX cloud-top distribution in Figure 4 suggested that this mode was associated with colder cloud tops (about 11 °C) than the LES second mode. Figure 7 cloud-top temperature distributions reveal a large variability of the distribution with time.

The stratification of water vapour around the flower cloud, as well as cloud-top height variability, is assessed by comparing the LES with the WALES profiles of humidity and the colocated WALES cloud mask (Figure 8), for the same seven time windows as in Figure 7. The extinction of the lidar signal due to the presence of cloud hydrometeors

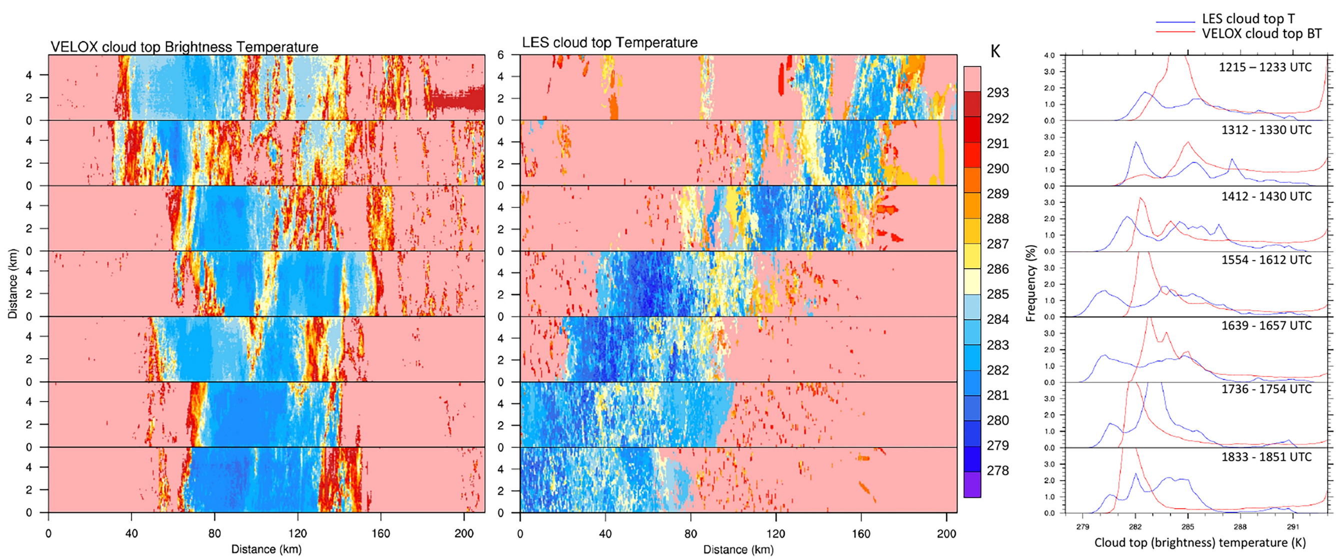

FIGURE 7 Evolution of cloud-top temperature: (left) using brightness temperature from VELOX broadband channel (between 7.7 and 12 μm) when passing over the flower-cloud south of the HALO circle (Figure 1), (middle) from LES using temperature of the highest grid cells where cloud liquid water mixing ratio exceeds 10^{-6} kg·kg^{-1}, and (right) cloud-top temperature distributions. From top to bottom, using VELOX measurements between 12:15 and 12:33, 13:12 and 13:30, 14:12 and 14:30, 15:54 and 16:12, 16:39 and 16:57, 17:36 and 17:54, 18:33 and 18:51 UTC, respectively. For LES, the output at the time in the middle of each time range is used [Colour figure can be viewed at wileyonlinelibrary.com]

1477870x, 2023, 750, Downloaded from https://rmets.onlinelibrary.wiley.com/doi/10.1002/qj.4409 by Portail BibCNRS INSU, Wiley Online Library on [25/10/2023]. See the Terms and Conditions (https://onlinelibrary.wiley.com/terms-and-conditions) on Wiley Online Library for rules of use; OA articles are governed by the applicable Creative Commons License

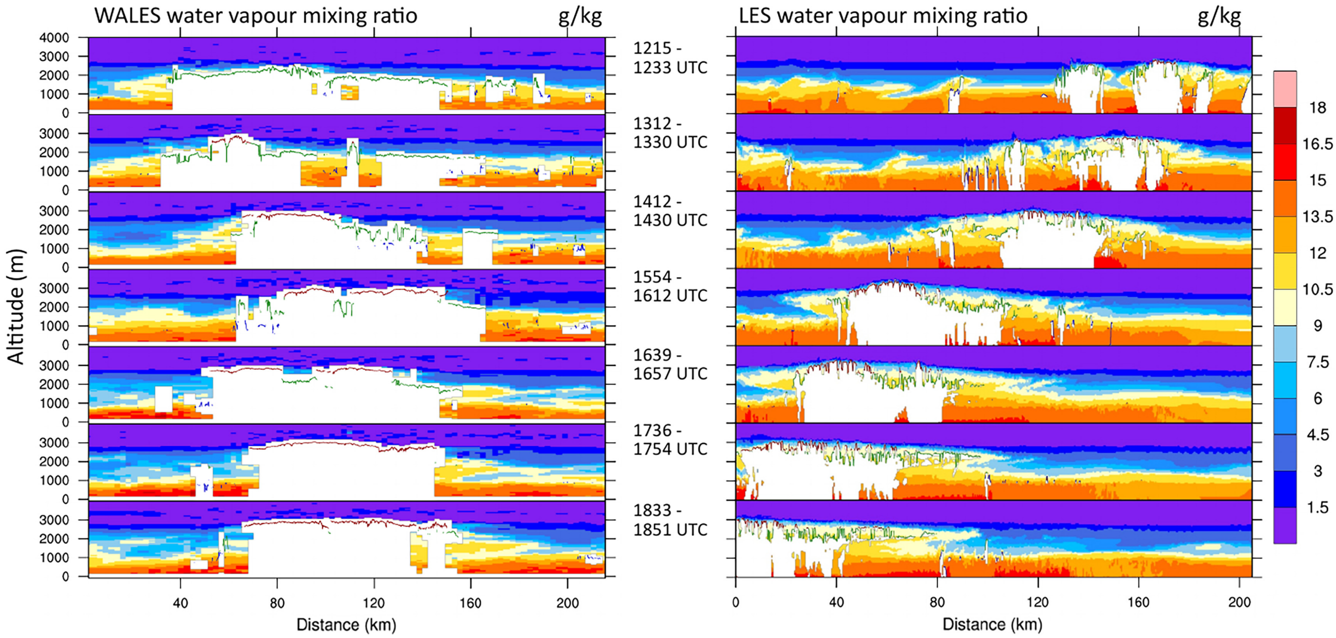

FIGURE 8 Evolution of the water-vapour field around the flower clouds and of the cloud-top altitude: (left) using WALES water-vapour profiles and WALES cloud mask, when HALO passed over the flower-cloud south of the circle (same as Figure 6), (right) using LES water-vapour field and altitudes of the highest grid cells where cloud liquid water mixing ratio exceeds 10^{-6} kg·kg^{-1}, along a zonal-vertical cross-section at y=67 km in the LES output, at the time in the middle of each time range used for WALES (like in Figure 6). Cloud top line is coloured depending on cloud-top altitude: blue below 1,300 m, green between 1,300 and 2,500 m and red above 2,500 m, to match the three modes of the cloud-top altitude distribution shown in Figure 4 [Colour figure can be viewed at wileyonlinelibrary.com]

is visible in white, and mimicked in the LES where the liquid water content is larger than 10^{-6} kg·kg^{-1}. In clear sky, the subcloud layer is deeper and drier in the LES than in the WALES observations; this is particularly visible after 1630 UTC and consistent with the comparison of composite vertical profiles in Figure 6. This is consistent with the deep, cold, and dry bias observed in the climatological evaluation of the forcing model AROME-OM (Beucher *et al.*, 2022), but further investigations are needed to determine whether the LES's deeper and drier subcloud layer is simply a heritage from AROME-OM or whether Meso-NH model contributes to this difference as well. Both the WALES measurements and the LES show a moist outflow from the flower cloud, about 1 km deep. This moist outflow is between 2 and 3 km altitude in the LES, and about 1 km lower in the WALES profiles. Concerning the cloud-top height variability, three modes of the WALES cloud-top distribution are visible, the second one with more altitude variations than the third, as in the LES. However, the LES highest cloud tops are not as flat as in the WALES cloud mask. This is consistent with the cloud-top altitude frequency distribution (Figure 4), for which the third mode in the WALES measurements is much more pronounced than in the LES, and with the cloud-top altitude distribution retrieved by specMACS (Figure S1 in Supporting Information), where large parts of the cloud tops cannot be retrieved, probably because of a lack of contrast in altitude.

In conclusion, the LES is able to produce a flower-cloud that is in line with the high-resolution observations on February 2, 2020 in terms of cloud fraction and cloud-top distribution, despite slightly too few of the highest clouds. Although the cloud-top height and temperature are more heterogeneous in the LES than in the WALES and VELOX observations, the simulated flower cloud has realistic characteristics.

4 | INVESTIGATION OF THE CONVECTIVE PROCESSES AND THEIR ORGANISATION

The convective processes at play in a flower cloud are investigated based on the LES fields. First, at the surface, cold pools and gust fronts are characterised. Then the vertical structure of the hydrometeor content, wind, and potential temperature gives further insight into the organisation of the cloud system. Finally, the LES fields are partitioned into two main classes: cloudy and clear-sky columns, and for each class further distinction is made between *updraft*, *cold-pool*, and *other* columns. Each of the

1477870x, 2023, 750, Downloaded from https://rmets.onlinelibrary.wiley.com/doi/10.1002/qj.4409 by Portail BibCNRS INS2I, Wiley Online Library on [25/10/2023]. See the Terms and Conditions (https://onlinelibrary.wiley.com/terms-and-conditions) on Wiley Online Library for rules of use; OA articles are governed by the applicable Creative Commons License

six categories is characterised and its contribution to the turbulent fluxes is computed.

4.1 | Cold pools and gust fronts at the surface

Cold pools correspond to pockets of cold, negatively buoyant air that sinks in the lower troposphere and spreads at the surface as a consequence of rain evaporation. Since the pioneering study of Zuidema *et al.* (2012), cold pools are suspected to play an important role in the organisation of trade-wind cumuli. Their systematic identification from the EUREC^{4}A atmospheric soundings (Touzé-Peiffer *et al.*, 2022) reveals that cold pools were present 7% of the time and characterised by colder (1 K), moister (1 g·kg^{-1}), and windier (2 m·s^{-1}) air than the environment. In the LES, cold pools leave a clear signature in the virtual potential temperature field at the surface (actually the values at 20 m altitude, the first model level, are represented in Figure 9). They are aggregated into a wide cluster, as large as the flower cloud. Fresh (recently formed and colder) cold pools are located at the cluster's western inner edge. At the western outer edge, some cold pools with larger virtual potential temperatures are vanishing. The imprints of cold pools are also visible in the zonal wind anomaly close to the surface. The westward wind is enhanced (reduced) in the western (eastern) half of the cold pools, consistent with the horizontal divergence of negatively buoyant air at the surface. The downward momentum transport from the free troposphere, where the trade winds are most intense, contributes to the intensification of the winds at the western edge of the cold pools. The wind intensification at the surface is expected to produce steeper

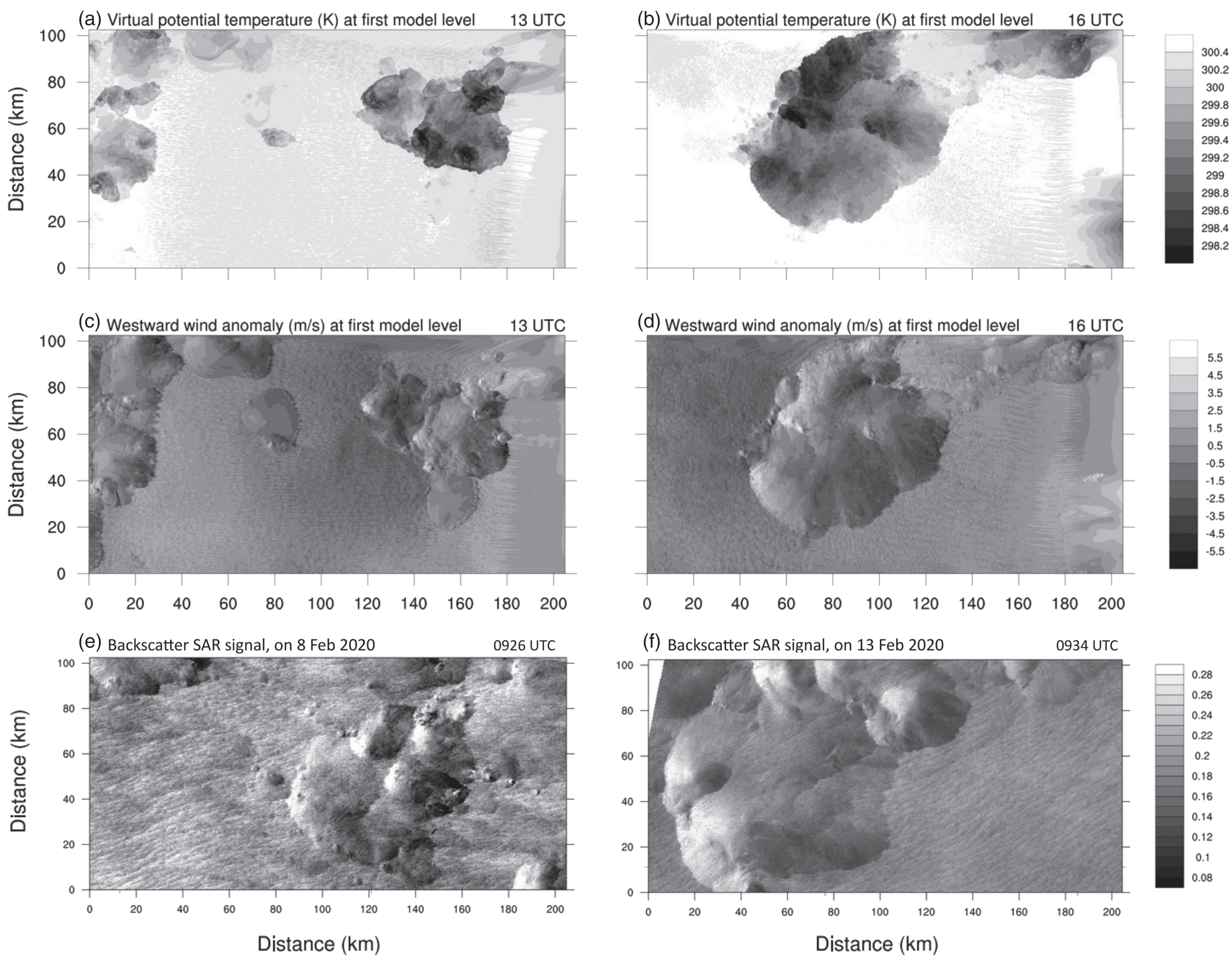

FIGURE 9 Evolution of cold pools, as seen with (a,b) the virtual potential temperature and (c,d) the westward wind anomaly $-(u - \bar{u})$, both at the first model level, that is, 20 m above sea level, at (a,c) 1300 UTC and (b,d) 1600 UTC. (e,f) Example of wide-swath SAR images showing surface roughness with a very similar pattern to that in (c,d), measurement on February 8 and 13, 2020 when the trade-wind clouds adopt a flower organisation like that on February 2, 2020

1477870x, 2023, 750, Downloaded from https://rmets.onlinelibrary.wiley.com/doi/10.1002/qj.4409 by Portail BibCNRS INSU, Wiley Online Library on [25/10/2023]. See the Terms and Conditions (https://onlinelibrary.wiley.com/terms-and-conditions) on Wiley Online Library for rules of use; OA articles are governed by the applicable Creative Commons License

small-scale waves on the sea surface and then increase the sea-surface roughness locally. This results in a stronger backscatter signal when measurements are taken from an active remote-sensing device such as SAR. The wide-swath SAR images (Figure 9e,f, from February 8 and 13, 2020, respectively, since no such image is available on February 2) reveal patterns in the sea-surface roughness (i.e. backscatter signal) that are consistent with the zonal wind anomalies associated with cold pools in the LES. This qualitatively confirms that the LES is producing cold pools with horizontal extent in agreement with observations. The presence of large cold pools is a first common characteristic shared between flower clouds and deep convective systems (e.g., Khairoutdinov *et al.*, 2009; Schlemmer and Hohenegger, 2014).

Cold pools are detected in the LES using two different methods: that described in Rochetin *et al.* (2021), hereafter R21, and that described in Touzé-Peiffer *et al.* (2022), hereafter T21. In short, R21 first detects so-called gust fronts as regions where the temperature drops by at least 10^{-3} K$\cdot$s^{-1}. Gust fronts are assumed to exhibit the virtual potential temperature range (this range of values is noted $[\theta_v]$) of the cold pools and their environment. Cold pools are then detected as regions where θ_v is lower than the first quartile of the $[\theta_v]$ range. The advantage of R21 is that gust fronts are detected, in addition to cold pools. Method T21 is simpler: it detects cold pools based on the mixed-layer depth only and leads to much larger cold pools than R21. It samples both the fresh cold pools detected by R21 (the lowest virtual potential temperature values) and their surroundings, made of cold-pool air that has already warmed up (Figure 10a). The gust fronts detected by R21 indeed sample the full range of virtual potential temperatures over the domain (Figure 10a), as well as regions with very intense wind anomalies (Figure 10b). R21 cold pools oversample nonzero instantaneous precipitation (Figure 10c) and have, surprisingly, the same distribution of wind anomalies as R21 gust fronts. In the rest of the study, the cold pools are detected using T21 only, as the detected cold pools encompass the whole area that one would associate with cold pools based on the surface fields (Figure 9), that is, up to the regions where secondary formation of clouds is observed, in line with the archetypal image of cold pools.

4.2 | Mesoscale circulation and structure of the cloud, rain, and updrafts

The organisation of the flower cloud is investigated further with vertical cross-sections. The location of the vertical cross-section shown in Figure 11 is selected in order to cross both clear-sky and cloudy regions, approximately at

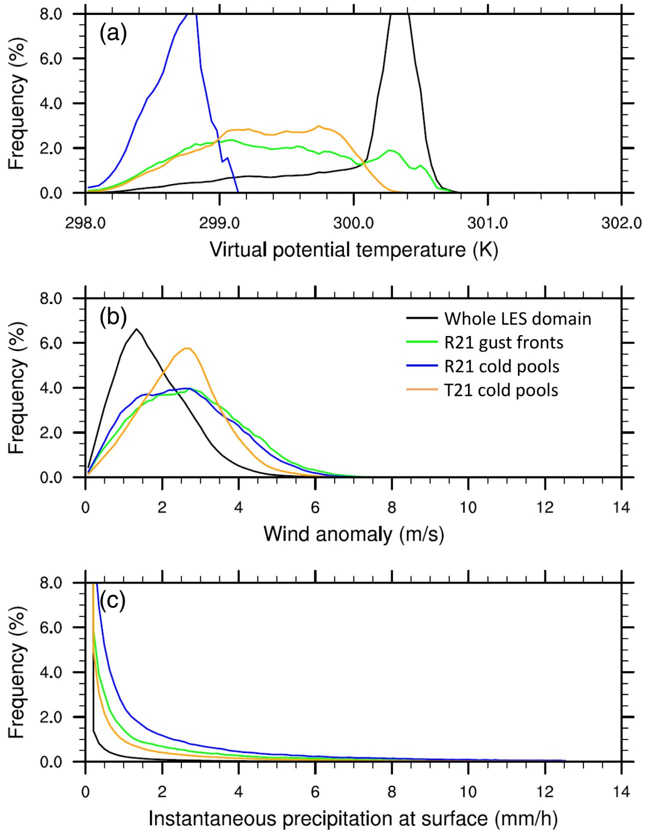

FIGURE 10 The distributions of (a) mixed-layer virtual potential temperature, (b) mixed-layer wind anomaly amplitude, and (c) surface instantaneous precipitation, over the full LES domain (black), over the gust fronts (green), and over the cold pools (blue and orange) detected by algorithms R21 and T21, respectively. The distributions are computed based on six simulation outputs, one every hour between 1300 and 1800 UTC [Colour figure can be viewed at wileyonlinelibrary.com]

the centre of the flower cloud. The cloud aggregate is about 1 km deep, with a western edge (from 45–55 km abscissa in Figure 11) characterised by a larger rain rate, deeper cloud, and lower cloud base (at 800 m altitude) than the rest of the cloud (Figure 11a). This part is named the *convective part*, with reference to deep mesoscale convective systems (MCSs: Houze *et al.*, 1980). Similarly, the region with higher cloud base and lighter rain is named the *stratiform part*. The mesoscale structure of the flower cloud is assessed with a 10-km running average of zonal wind anomalies, with respect to the domain average zonal wind profile (Figure 11b). It exhibits a mesoscale circulation typical of deep mesoscale convective systems (Zipser, 1977; Houze, 2004): outflow near the cloud top and inflow in the low troposphere, on the western side of the system, except that this circulation tops at 3 km altitude. The outflow in the low troposphere on the upwind (eastern) side of the system is due to cold pools. The thermal structure (Figure 11c) indicates low potential temperature at

1477870x, 2023, 750, Downloaded from https://rmets.onlinelibrary.wiley.com/doi/10.1002/qj.4409 by Portail BibCNRS INSU, Wiley Online Library on [25/10/2023]. See the Terms and Conditions (https://onlinelibrary.wiley.com/terms-and-conditions) on Wiley Online Library for rules of use; OA articles are governed by the applicable Creative Commons License

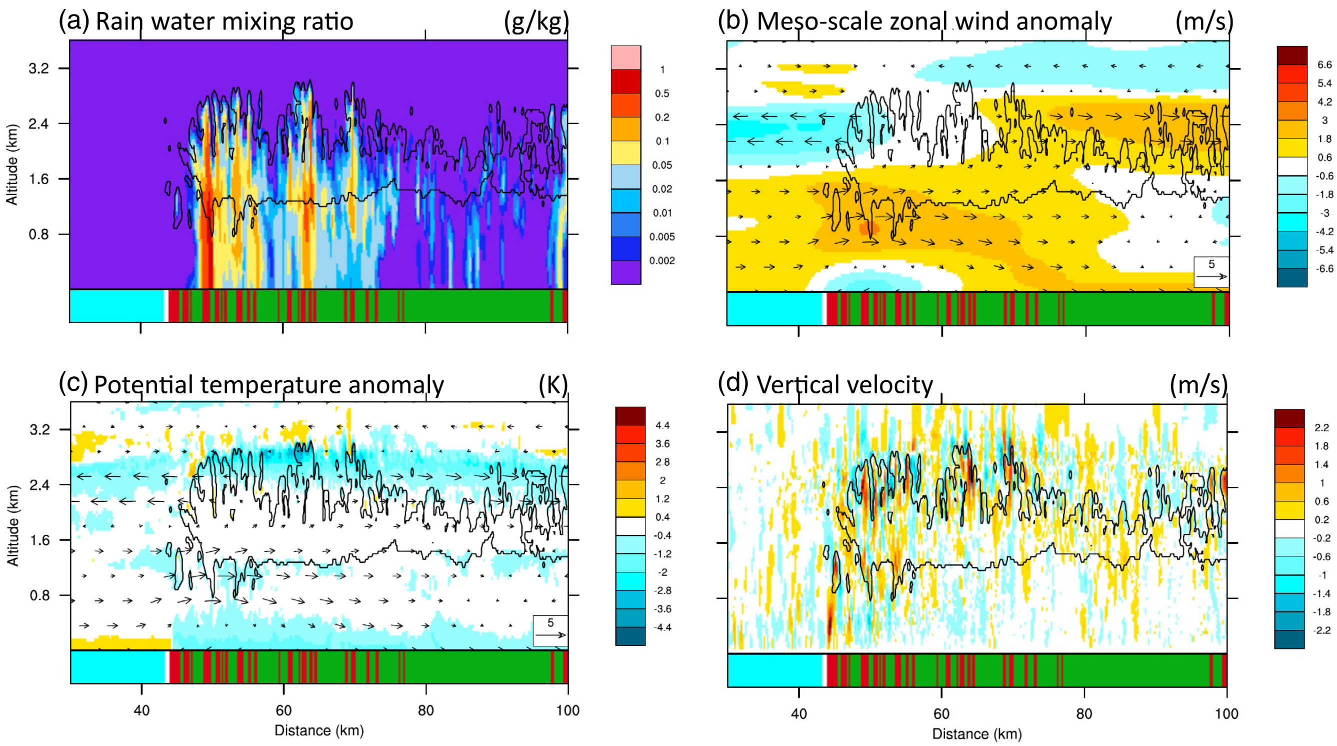

FIGURE 11 West–east vertical cross-sections in the LES flower cloud at 1600 UTC, with shading for: (a) rain water mixing ratio ($g \cdot kg^{-1}$), (b) mesoscale zonal wind anomaly ($m \cdot s^{-1}$), (c) potential temperature anomaly (K), and (d) vertical velocity ($m \cdot s^{-1}$). In all panels the black contour is for a cloud liquid water mixing ratio of 10^{-6} $kg \cdot kg^{-1}$. The stripes below the panels indicate the categories of the columns in the cross-sections with the same colour code as in Figure 12. In panels (b) and (c), the arrows represent the mesoscale zonal and vertical wind anomaly in the vertical cross-section. Note that, by convention, zonal wind u is positive toward the east [Colour figure can be viewed at wileyonlinelibrary.com]

the surface below the cloud, associated with cold pools, and at the cloud top, in the region of the trade-wind inversion. The latter is a signature of air coming from the cloud at lower altitude. The vertical wind distribution (Figure 11d) reveals convective-scale structures, i.e. with a size of 1 km or narrower. Updrafts in the subcloud layer are seen out of the flower cloud (west of $x = 47$ km), while they are shut down in the cold pools (much fewer east of $x = 47$ km). In the western edge of the system (for x between 43 and 47 km), more intense subcloud-layer updrafts develop with small clouds at their top. In the flower cloud, the updrafts are most intense near the cloud base and the cloud top in the convective part (x between 47 and 56 km) and near the cloud top only in the stratiform part ($x > 56$ km). Vertical velocities near the cloud top are also fostered by the trade-wind inversion that promotes the wave activity. Strong downdrafts (with more than 1 $m \cdot s^{-1}$ downward velocity), either in clear sky or in cloudy air, surround the updrafts near the cloud tops; they are interpreted as *subsiding shells*. Such circulations are usually found near the lateral boundary of the shallow clouds (e.g., Rodts *et al.*, 2003), but they are also found at the top of congestus (Strauss *et al.*, 2021) and deep convective systems (Glenn and Krueger, 2014; Dauhut *et al.*, 2016). The presence of a mesoscale circulation, and of a convective part and a stratiform part with contrasted microphysical properties, is another characteristic that flower clouds share with deep MCSs (e.g., Houze, 2004; Barnes and Houze, 2014).

4.3 | Updraft and cold-pool composites and their contribution to the turbulent fluxes

The convective processes at play in a flower cloud are investigated further by partitioning the simulated fields. This partition is 2D: it differentiates the columns of the LES (the columns considered here are one grid point wide). First, clear-sky and cloudy columns are distinguished based on a threshold on LWP of 2×10^{-5} $kg \cdot m^{-2}$. The *updraft columns* are columns where the maximal vertical velocity is larger than $+1$ $m \cdot s^{-1}$. The remaining columns are separated between *cold-pool columns*, where the mixed-layer depth is lower than 400 m following T21, and *other columns*.

1477870x, 2023, 750, Downloaded from https://rmets.onlinelibrary.wiley.com/doi/10.1002/qj.4409 by Portail BibCNRS INS2I, Wiley Online Library on [25/10/2023]. See the Terms and Conditions (https://onlinelibrary.wiley.com/terms-and-conditions) on Wiley Online Library for rules of use; OA articles are governed by the applicable Creative Commons License

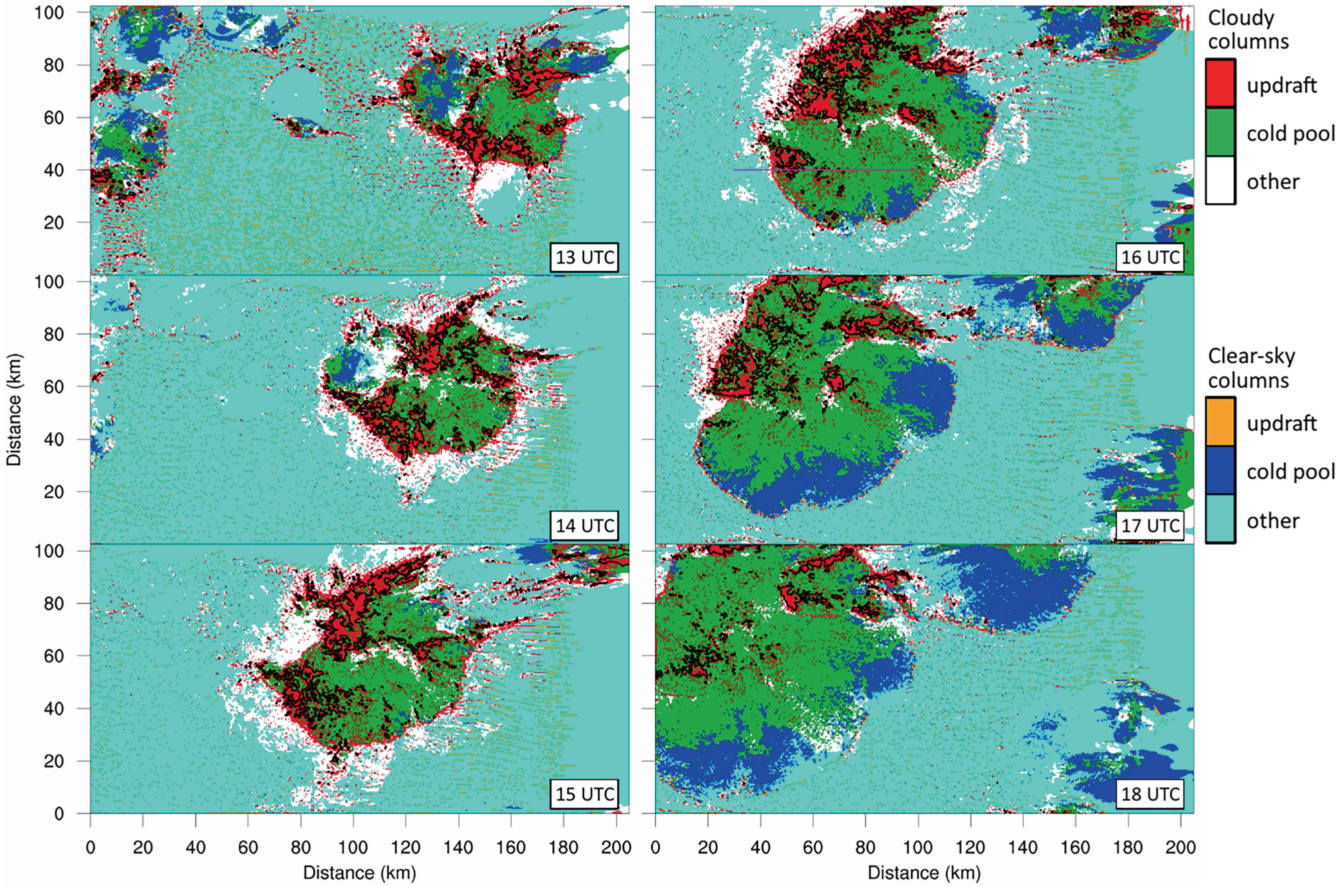

FIGURE 12 Maps of the partition, every hour from top to bottom and from left to right. Red (yellow), green (dark blue), and white (cyan) stand for the updraft column, cold-pool column, and other column, all in cloudy (clear-sky) areas, respectively. A threshold of 2×10^{-5} kg·m^{-2} in LWP is used to distinguish cloudy from clear-sky areas. A rain water mixing ratio of 0.1 g·kg^{-1} at 780 m above sea level is contoured in black. Table 2 gives the percentage of the domain covered by each category [Colour figure can be viewed at wileyonlinelibrary.com]

TABLE 2 Evolution of the area fraction for each column category. Time is in UTC and fractions are in %

	Cloudy			Clear-sky		
Time	**Updraft**	**Cold pool**	**Other**	**Updraft**	**Cold pool**	**Other**
1300	10	7.8	8.3	7.6	4.1	62
1400	7.5	6.7	11	3	0.74	71
1500	10	11	13	2.8	0.73	62
1600	9.8	17	10	2.8	3.4	56
1700	7.4	23	6.9	2.5	11	49
1800	5.2	25	5	2.3	14	48
avg	8.3	15.1	9.0	3.5	5.7	58

The LES partition evolves with time (Figure 12 and Table 2). On average over the hourly output between 1300 and 1800 UTC, the two most common categories are cloudy cold pools (15%) and clear-sky other columns (58%). The fraction of updraft columns remains roughly constant during the simulation (near 10% in clouds and 3% in clear sky), while the fraction of cold-pool columns grows at the expense of the other columns. The reason why the updraft column fraction remains roughly constant needs further investigation. It translates the fact that new

1477870x, 2023, 750, Downloaded from https://rmets.onlinelibrary.wiley.com/doi/10.1002/qj.4409 by Portail BibCNRS INS2I, Wiley Online Library on [25/10/2023]. See the Terms and Conditions (https://onlinelibrary.wiley.com/terms-and-conditions) on Wiley Online Library for rules of use; OA articles are governed by the applicable Creative Commons License

updrafts are generated as fast as previous updrafts dissipate, and that cold-pool expansion organizes the updraft columns but does not affect their number at this stage of the flower-cloud life cycle. A tentative explanation could be that the convective activity reaches some kind of equilibrium at these space and time scales (hundreds of km, hours), defined by the large-scale conditions of the atmosphere and the mesoscale organisation of the updrafts. Cloudy updrafts developed preferentially on the western inner edge of the flower cloud. They organise into an arc with time. In the western outer edge, clouds are shallower. They are growing and achieve vertical velocities larger than $+1\,\mathrm{m{\cdot}s^{-1}}$ later. This aspect again makes flower clouds similar to MCSs, especially the ones observed during the Global Atmospheric Research Program Atlantic Tropical Experiment (GATE) campaign (LeMone *et al.*, 1984). East of the cloudy updrafts, a very large cold-pool region develops, growing steadily from 8 to 25% of the domain from 1300–1800 UTC (i.e. an increase from 1,600 to 5,200 $\mathrm{km^2}$ in 5 hr). Until 1600 UTC, cloudy updrafts also develop east of the flower cloud, potentially supplying the flower cloud on its eastern edge. From 1600 UTC onward, the cold-pool region is actually larger than the flower cloud. Whereas clear-sky updrafts populate the regions out of the cold pools, no updraft is found inside the clear-sky cold-pool region. This does not mean that the cold pools are in fully stable conditions, since turbulence is still active in the lowest 100–200 m (as indicated by large values of subgrid turbulent kinetic energy close to the surface, not shown), but that the vertical motions that develop in the cold pools are weaker than $1\,\mathrm{m{\cdot}s^{-1}}$. The subcloud layer then needs time to recover and host updrafts reaching $1\,\mathrm{m{\cdot}s^{-1}}$, in line with Zuidema *et al.* (2012). Cloudy updrafts are also found in isolated spots in the middle of the cold-pool region, potentially due to cold-pool collisions below the flower clouds, fostering humidity horizontal convergence and updraft development. The rain mixing ratio below the cloud is largest in cloudy updraft columns and lighter in cloudy cold-pool regions.

Composite profiles of the six column categories (average profiles over all the columns of each category, Figure 13) indicate that the clear-sky updraft columns sample the clear-sky subcloud-layer strong thermals well, with near-zero vertical velocity above the subcloud layer. Cloudy updraft columns host less intense upward velocities than clear-sky updrafts; this is because the composite profile averages cloudy updrafts that are at different altitudes. Other columns exhibit negative vertical velocities on average. Cold-pool columns do not show stronger downward motions in the subcloud layer than clear-sky other columns, as one would have expected. This might be due to the fact that the cold pools detected are on average mature cold pools, which subside less and spread more horizontally than newly generated ones. The average $0.05\,\mathrm{m{\cdot}s^{-1}}$ downward motion in clear-sky other columns is consistent with the mesoscale downdraft outside flower clouds highlighted by Narenpitak *et al.* (2021) and, from a larger perspective, the mesoscale downdraft developed outside at the mature stage of a MCS (e.g. those found in composites of the large MCSs called mesoscale convective complexes: Cotton *et al.*, 1989). However, cloudy cold-pool columns show strong negative vertical velocities near the cloud top. This is due to the subsiding shells that develop in the neighbourhood of updrafts near the cloud top (Figure 11d). These subsiding shells are accidentally sampled by the cloudy cold-pool category of the partition, because both subsiding shells and cold pools develop in the vicinity of cloudy updrafts. Despite being sampled by the same column category, subsiding shells do not necessarily supply cold pools with negatively buoyant air. Indeed, there is a huge altitude gap between these two types of circulation: subsiding shells develop above 2 km altitude (Figure 11d) whereas cold pools are below 400 m altitude, without evidence of continuity between the two. Most of the cold-pool supply seems instead to come from the evaporation of rain in the cloudy updraft area, west of the flower cloud (Figure 11). The cloudy updraft columns contain the most cloud liquid water and rain water. The cloudy cold-pool columns contain one third less cloud liquid water and five times less rain water in comparison, but still much more than the cloudy other columns that correspond to the edge of the flower cloud. These contrasts are consistent with the ones between convective and stratiform parts in a deep MCS (e.g., Houze, 1977; Zipser, 1977).

The contributions of the six categories of columns to the turbulent fluxes of sensible heat, humidity, and zonal momentum are computed and averaged over the hourly output of the LES between 1300 and 1800 UTC (Figure 14). Total fluxes are shown; they are the sum of the explicit and subgrid fluxes. Note that subgrid fluxes contribute significantly near the surface (below 200 m) only, and to a lesser extent to the sensible heat flux in the cloud layer (up to $-3 \times 10^{-3}\,\mathrm{K{\cdot}m{\cdot}s^{-1}}$). The upward turbulent sensible heat flux (Figure 14a) is driven by the cloudy updraft columns above the subcloud layer up to about 2,300 m altitude. Above and up to the cloud top, the subsiding shells sampled by the cloudy cold-pool category contribute the most to the upward turbulent sensible heat flux, while the cloudy updrafts have a strong negative contribution that partly compensates for the upward sensible heat transport, in line with, for example, Davini *et al.* (2017). Since the subsiding shells have negative average vertical velocities and the updrafts have positive ones, their contribution to the turbulent sensible heat flux at the cloud top is due to air masses with low potential temperatures. They are then

1477870x, 2023, 750, Downloaded from https://rmets.onlinelibrary.wiley.com/doi/10.1002/qj.4409 by Portail BibCNRS INSU, Wiley Online Library on [25/10/2023]. See the Terms and Conditions (https://onlinelibrary.wiley.com/terms-and-conditions) on Wiley Online Library for rules of use; OA articles are governed by the applicable Creative Commons License

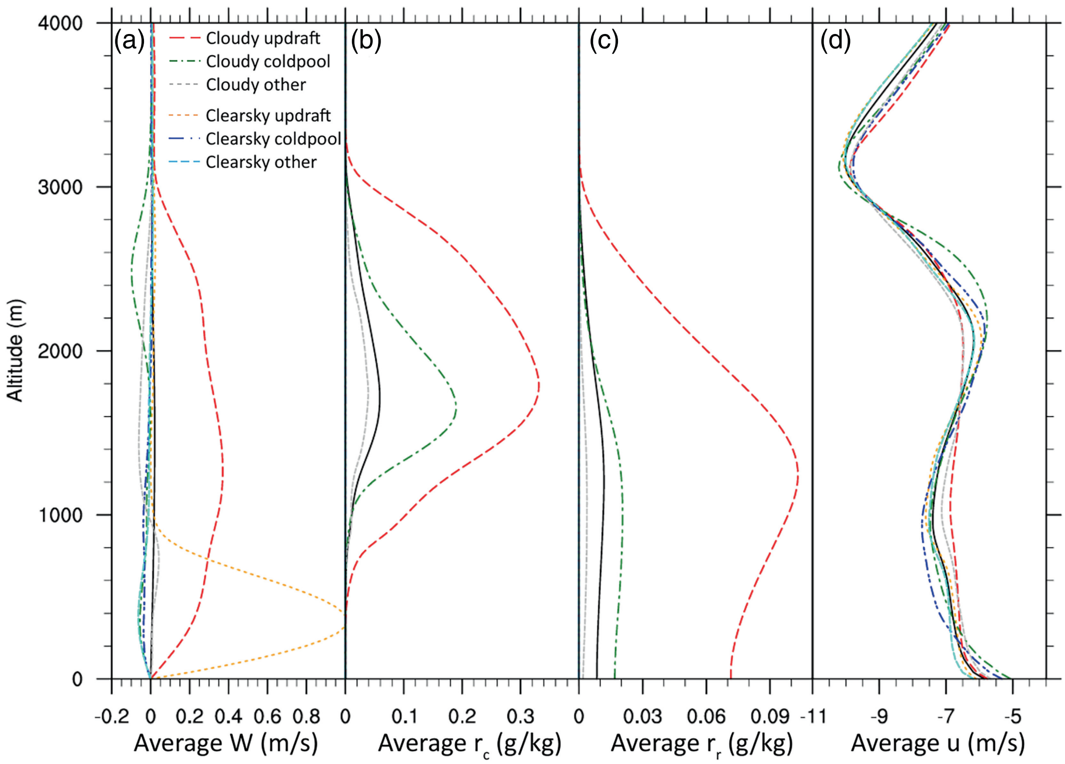

FIGURE 13 Composite profiles for each category of the partition: (a) average vertical velocity ($m \cdot s^{-1}$), (b) average cloud liquid water mixing ratio ($g \cdot kg^{-1}$), (c) average rain water mixing ratio ($g \cdot kg^{-1}$), and (d) average zonal velocity ($m \cdot s^{-1}$, positive eastward by convention). The domain average is in black [Colour figure can be viewed at wileyonlinelibrary.com]

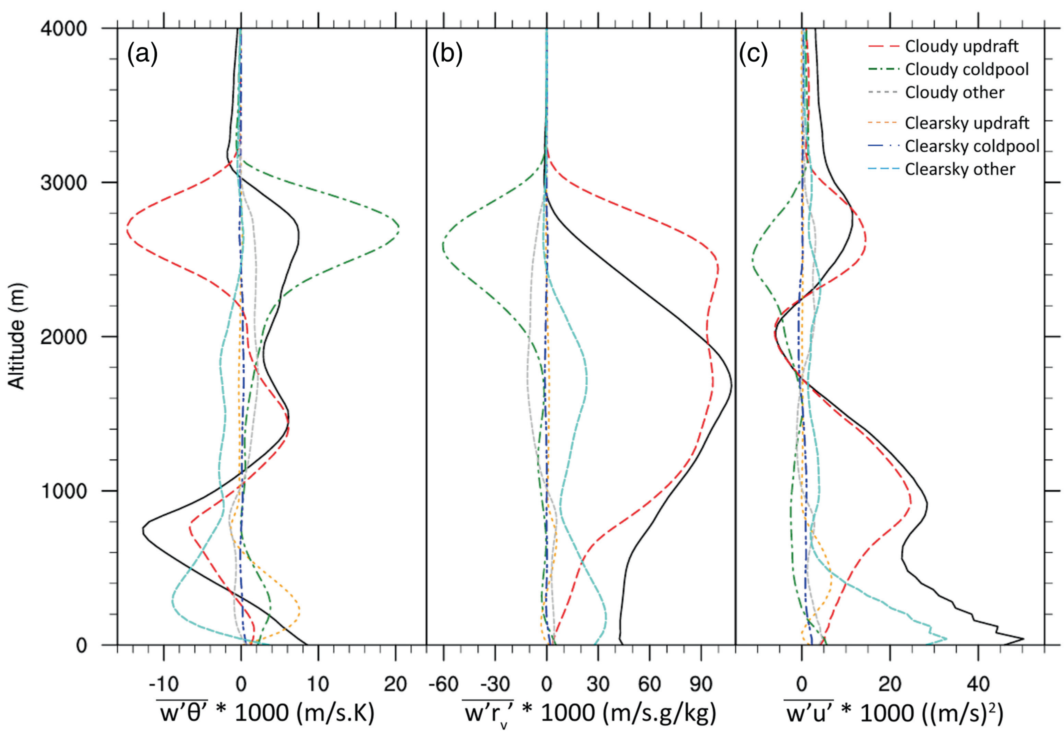

FIGURE 14 Contribution of each category of the partition to the vertical turbulent transport of (a) sensible heat, (b) water vapour, and (c) zonal momentum (positive for upward transport of eastward momentum and downward transport of westward momentum). The domain average is in black [Colour figure can be viewed at wileyonlinelibrary.com]

1477870x, 2023, 750, Downloaded from https://rmets.onlinelibrary.wiley.com/doi/10.1002/qj.4409 by Portail BibCNRS INSU, Wiley Online Library on [25/10/2023]. See the Terms and Conditions (https://onlinelibrary.wiley.com/terms-and-conditions) on Wiley Online Library for rules of use; OA articles are governed by the applicable Creative Commons License

made of air that originates from low altitudes, ascends in the cloud beyond its level of neutral buoyancy (overhoots), and subsides back to this level. Below, in the lower half of the subcloud layer, the turbulent sensible heat transport is upward, with positive contributions from all updraft columns and cloudy cold pools and a negative contribution from clear-sky other columns that is consistent in terms of amplitude and vertical variations with the fair-weather sensible heat flux measured in situ during the GATE campaign (Nicholls and Lemone, 1980). In the current study, this negative contribution is due to warm subsidence that dominates this category (Figure 13a). Weak subcloud thermals (with maximal velocity about $0.25\,\mathrm{m\cdot s^{-1}}$) also populate the clear-sky other columns but they are fewer (40% of this category versus 60% for subsidence). They are associated with theta anomalys that are virtually the same as the subsidence (barely less warm), so the resulting negative sensible heat transport is a consequence of the difference in frequency. In the upper half of the subcloud layer, the cloudy updraft columns and clear-sky other columns contribute the most to the downward sensible heat turbulent flux. The upward turbulent humidity flux and upward turbulent zonal momentum flux (Figure 14b,c) are driven mostly by cloudy updrafts. Near the cloud top only, the subsiding shells partly compensate for the upward turbulent humidity and zonal momentum fluxes, and in the subcloud layer the clear-sky other columns contribute more than the cloudy updraft columns to the upward turbulent humidity and zonal momentum fluxes. Significant contributions of the cloudy updrafts of a flower cloud to the turbulent fluxes, including the momentum turbulent fluxes, is another common point with deep MCSs (e.g., LeMone, 1983; Barthe *et al.*, 2010). Comparison with the zonal wind profile (Figure 13d) indicates that the zonal momentum flux is downgradient up to 0.9 km and between 1.7 and 3.2 km altitudes, and against the zonal wind gradient between 0.9 and 1.7 km altitudes. Such a transport against the zonal wind gradient makes the flower cloud similar to the quasi-two-dimensional deep convective bands observed during the GATE campaign (LeMone, 1983). The reasons for this similarity remain to be explored.

5 DISCUSSION

The investigation of the processes at play in flower clouds based on the LES indicate that these clouds share several similarities with deep mesoscale convective systems (Figure 15). The cloud cluster is made of three distinct regions (Figure 11): the *convective part* that hosts most of the cloudy updrafts, with large rain rate, the highest cloud tops, and the lowest cloud base (at 800 m altitude, the top of the subcloud layer), the *stratiform part* that is sampled by detecting cold pools, with higher cloud base and lighter rain, and the *remainder of the cloud cluster*. Similarly to deep mesoscale convective systems, a mesoscale circulation (e.g., Houze, 2004) takes place at the scale of the flower cloud, supplying the system with moist air from the lowest 1.6 km—twice the depth of the subcloud layer. The rising branch of this mesoscale circulation is made of the convective part of the flower cloud. The mesoscale outflow takes place both west and east of the flower cloud, between 1.6 and 2.7 km altitude.

The fourth branch of the mesoscale circulation, outward in the lowest 1,600 to 400 m, is driven by the spreading cold pool below the flower cloud (Figures 9 and 15). It is worth noting here that this cold pool is wide enough to contribute significantly to the mesoscale circulation. The identification of cold pools using R21 (not shown) indicates that it is supplied with cold air near the convective part, where the rain rates are the most intense. This gigantic cold pool, more than 80 km wide (30% wider than the largest cold pool reported in Zuidema *et al.*, 2012), is suspected to give a circular shape to the flower cloud, as the cloudy updrafts that supply the cloud develop preferentially at its edge (see Rotunno *et al.*, 1988 for more details on this later process). Furthermore, this wide cold pool can be seen as the aggregate of several smaller cold pools that are generated continuously during the life cycle of the flower cloud. Both the size of this cold pool and the aggregate structure are confirmed with SAR observations when available (the ones shown in Figure 9 are from two other days with similar cloud organisation). In line with the clear-sky LES of Ayet *et al.* (2021), this latter point stresses how valuable the SAR observations are to investigate the circulation in the marine subcloud layer, in particular below the cloud clusters. As in the case of the flower cloud investigated here, these circulations are key for the organisation of clouds. Further investigations are necessary to understand how SAR observations could help to determine the cold-pool dynamics (collisions, individual life cycle, etc.). Two questions remain concerning cold pools: what is their role in the initiation of flower clouds? And what is their role in the mesoscale circulation conceptualised by Narenpitak *et al.* (2021)? Scrutinizing *GOES-16* visible movies suggests that cold pools play a substantial role in the initialisation of flower clouds, which seem to develop where two or even three cold pools collide, confirming theoretical studies like those of Haerter *et al.* (2019) and Meyer and Haerter (2020) and suggesting another similarity with deep convective systems, which develop preferentially where convergence lines (due to two cold pools for instance) collide (e.g., Wilson and Schreiber, 1986). The question remains open as to whether only cold pools generated by rain-evaporation are at play or whether radiatively driven shallow circulations (Naumann *et al.*,

1477870x, 2023, 750, Downloaded from https://rmets.onlinelibrary.wiley.com/doi/10.1002/qj.4409 by Portail BibCNRS INSU, Wiley Online Library on [25/10/2023]. See the Terms and Conditions (https://onlinelibrary.wiley.com/terms-and-conditions) on Wiley Online Library for rules of use; OA articles are governed by the applicable Creative Commons License

1477870x, 2023, 750, Downloaded from https://rmets.onlinelibrary.wiley.com/doi/10.1002/qj.4409 by Portail BibCNRS INSU, Wiley Online Library on [25/10/2023]. See the Terms and Conditions (https://onlinelibrary.wiley.com/terms-and-conditions) on Wiley Online Library for rules of use; OA articles are governed by the applicable Creative Commons License

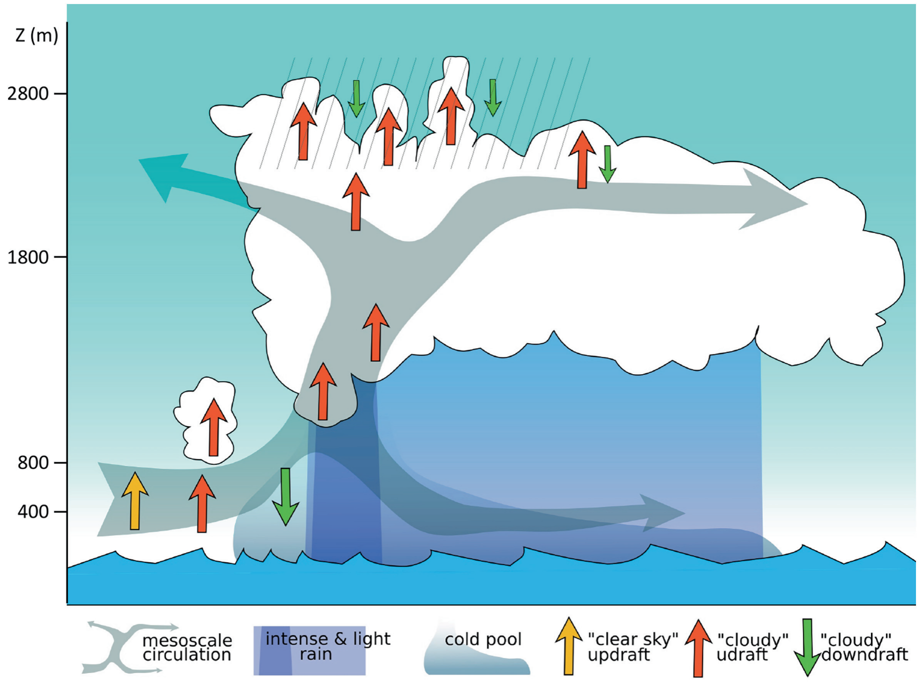

FIGURE 15 Schematic of a vertical cross-section through a flower cloud, along the trade-wind direction. The colours of the updrafts and downdrafts are consistent with the column category in which they are identified (Figure 12): clear-sky updraft (yellow), cloudy updraft (red), cloudy cold pool (green). The hatched area denotes the region where the agreement between LES and observation is the lowest. Small arrows are used to denote subsiding shells and distinguish them from cold pools. Sea-surface roughness is nonuniform to illustrate the impact of cold pools [Colour figure can be viewed at wileyonlinelibrary.com]

2017) also contribute to the dynamics of flower clouds. The same LES was performed without the temperature tendencies due to radiation (not shown). It produced as many cold pools, and a flower cloud as large as the one presented in this study. This suggests that it is mainly cold pools driven by rain evaporation that contribute to the convective dynamics once flower clouds are developed.

The partition of the LES fields highlights the very large contribution of cloudy updraft columns to the turbulent vertical fluxes of sensible heat, moisture, and momentum, although they cover only 8% of the domain on average (Figure 13, red arrows in Figure 15). Qualitative comparisons between the vertical cross-sections of the water-vapour field from LES and WALES (Figure 8) indicate, however, that the detrainment of moisture around flower clouds might be too high in the LES (above 2 km altitude versus below this altitude in the observations). Several hypotheses might explain such a difference. The first two are linked directly to dynamical considerations: too many updrafts transport moisture beyond 2 km, or too little compensation of the updraft transport happens above 2 km. The former hypothesis seems invalid, since the comparison of cloud-top altitudes (Figure 4) indicates that the LES produces too few highest cloud tops. The latter hypothesis is not satisfying either, since the compensating circulations, subsiding shells, are indeed at play in the LES, but probably stronger than in reality, given the too-disturbed simulated cloud tops in Figures 7 and 8. Other hypotheses might then be formulated: is the mixing by turbulent eddies strong enough in the LES to detrain moisture below 2 km altitude? Are the microphysical processes well represented near the trade-wind inversion, in the highest cloud tops that seem to dissipate less in the observation than in the LES? Radiation seems to play a secondary role, since in the test simulation without the radiative tendencies (not shown) the flower cloud develops similarly to the control LES, with nonsignificant changes in shape or size. The test simulation without radiative tendencies produces a slightly more pronounced highest cloud-top mode, but at lower altitude than the LES presented here.

Moist anomalies in the free troposphere are present in both the LES and the WALES observations, even far away from the cloud cluster. It is unclear to what extent these anomalies are remnants of previously developed flower clouds, or smaller clouds. However, the flower cloud in the LES developed preferentially in one wide moist anomaly that was present in the initial field. This makes the moist anomaly potentially key in driving flower-cloud development. Narenpitak *et al.* (2021) highlighted how important the heterogeneities in the moisture field are and suggested that they were the results of mesoscale circulations that take place at the scale of each flower cloud. Such a mesoscale circulation makes the wet regions wetter and the dry ones drier, and this effect is even more pronounced when large-scale upward velocity is present in the free troposphere. Independently of flower clouds, Bretherton and Blossey (2017) suggest that a mesoscale circulation can develop spontaneously in a homogeneous environment on a time-scale of about 15 hr solely because of gross moist instability (convection makes wet regions wetter). Such a mechanism is then a candidate to explain mesoscale humidity heterogeneities over the oceans. Testing how much flower clouds are dependent on the mesoscale heterogeneities already present in the moisture field at their initialisation and on their amplitudes is something left for future work.

6 | CONCLUSION

One flower-cloud system that developed east of the Barbados Island is simulated for 7 hours, from 1200–1900 UTC on February 2, 2020. The LES, produced with the nonhydrostatic model Meso-NH and with 100-m (40-m) uniform horizontal (vertical) grid spacing, is evaluated using HALO aircraft measurements from the EUREC^{4}A field campaign, *GOES* geostationary satellite measurements, and *Sentinel* low-Earth-orbiting satellite SAR measurements. The simulated flower cloud exhibits characteristics similar to the observed ones on February 2, 2020: increasing size from about 50 km width at 1200 UTC to 100 km at 1600 UTC, three modes in the cloud-top altitude distribution, cloud tops that become colder during the day, and a moist detrainment layer in the clear sky nearby. The simulated wind anomalies at the surface show a pattern similar to the surface roughness observed by spaceborne SAR. Some differences exist, however: the LES produces less frequent highest cloud tops than the observed clouds, the height of the LES highest cloud tops is less homogeneous than in the lidar observations, the most frequent PW value is lower in the LES than in the radiometer measurements, the moist detrainment layer is higher in the LES than in the lidar vertical cross-section, and the free troposphere above the cloud tops happens to be moister and colder than observed by the dropsondes.

A mesoscale circulation is developed at the scale of the flower cloud, upward at the western inner edge of the flower cloud, the *convective part*, where most cloudy updrafts are located, along with the highest cloud tops and the largest rain rates. A 1,600-m deep inflow layer above the surface supplies the flower cloud from the west, and an 800-m deep outflow layer hosts strong divergence at the cloud top. Eastward near-surface outflow on the eastern side of the flower cloud is associated with large cold pools. Similarly to a deep MCS, a *stratiform part* can be defined east of the convective part, above cold pools at the surface and characterised by lighter rain rates. Within this mesoscale circulation, convective-scale circulations are taking place. Many updrafts are found in the subcloud layer west of the flower cloud. Deeper updrafts that extend from the surface into the free troposphere develop in the convective part. In the stratiform part, most updrafts are near the cloud top. In both parts of the flower cloud, the updrafts near the cloud top are surrounded by strong downdrafts that are interpreted as subsiding shells.

The investigation of the convective processes at play is led with a partition of the LES 3D fields, in order to distinguish clear-sky from cloudy columns and, within each of these two classes, the updraft columns, cold-pool columns, and other columns. The cloudy updraft columns are organised in an arc on the western inner edge of the flower cloud, with a pattern similar to the highest cloud tops. These columns are associated with the highest rain rates and the largest cloud liquid water content. East of them, the cold-pool columns cover a zone as large as the flower cloud that grows during the period of simulation. In the second half of the simulation, the cold-pool zone is actually larger than the flower cloud. Clear-sky cold pools spread to the south and east of the flower cloud. The composite profiles for all categories reveal that the clear-sky updraft columns sample the subcloud layer thermals well, and the cloudy cold-pool category accidentally samples subsiding shells in the upper part of the cloud, because both cold pools and subsiding shells develop in the vicinity of cloudy updrafts. The cloudy updrafts drive the vertical turbulent fluxes of humidity, zonal momentum, and to a lesser extent the vertical turbulent flux of sensible heat. The subsiding shells drive the highest part of the upward turbulent flux of sensible heat, and partly compensate the upward ones of humidity and zonal momentum. In the subcloud layer, clear-sky updrafts and other columns contribute to all fluxes.

The present study illustrates the wealth gained through the combination of LES with high-resolution observations from the EUREC^{4}A campaign to investigate processes governing the organisation of trade-wind clouds. The role of cold pools deserves to be investigated in contrasted study cases showing, for instance, a gravel organisation. Future investigations are planned to address the sensitivity of processes leading to flower organisations to the stability of the low atmosphere and the amplitude and size of pre-existing environmental heterogeneities.

AUTHOR CONTRIBUTIONS

Thibaut Dauhut: conceptualization; investigation; methodology; project administration; supervision; visualization; writing – original draft; writing – review and editing. **Fleur Couvreux:** conceptualization; funding acquisition; supervision; writing – review and editing. **Dominique Bouniol:** conceptualization; supervision; writing – review and editing. **Florent Beucher:** conceptualization; writing – review and editing. **Lea Volkmer:** data curation; visualization; writing – review and editing. **Veronika Pörtge:** data curation; writing – review and editing. **Michael Schäfer:** data curation; writing – review

1477870x, 2023, 750, Downloaded from https://rmets.onlinelibrary.wiley.com/doi/10.1002/qj.4409 by Portail BibCNRS INSU, Wiley Online Library on [25/10/2023]. See the Terms and Conditions (https://onlinelibrary.wiley.com/terms-and-conditions) on Wiley Online Library for rules of use; OA articles are governed by the applicable Creative Commons License

1477870x, 2023, 750, Downloaded from https://rmets.onlinelibrary.wiley.com/doi/10.1002/qj.4409 by Portail BibCNRS INSU, Wiley Online Library on [25/10/2023]. See the Terms and Conditions (https://onlinelibrary.wiley.com/terms-and-conditions) on Wiley Online Library for rules of use; OA articles are governed by the applicable Creative Commons License

and editing. **Alex Ayet:** writing – review and editing. **Pierre-Etienne Brilouet:** writing – review and editing. **Marek Jacob:** data curation; writing – review and editing. **Martin Wirth:** data curation.

ACKNOWLEDGEMENTS

This work was funded by the European CONSTRAIN project. The HALO observational products are available on the AERIS data portal (https://observations.ipsl.fr/aeris/eurec4a-data/AIRCRAFT/HALO/), as well as the hourly outputs from Meso-NH LES (doi:10.25326/368, https://observations.ipsl.fr/aeris/eurec4a-data/SIMULATIONS/). The *GOES-16* measurements are available online (https://console.cloud.google.com/storage/browser/gcp-public-data-goes-16/ABI-L2-CMIPF). A.A. and P.-E.B. were funded by CNES postdoctoral grants. This work was partly supported by CNES through the PROCONUM project, by the Max Planck Society and the DFG (Deutsche Forschungsgemeinschaft, German Research Foundation) through the HALO Priority Program SPP 1294 "Atmospheric and Earth System Research with the Research Aircraft HALO (High Altitude and Long Range Research Aircraft)". The authors warmly thank Margaret A. LeMone and an anonymous reviewer for their interesting comments, which contributed to improving the article.

ORCID

Thibaut Dauhut https://orcid.org/0000-0002-5468-3818
Fleur Couvreux https://orcid.org/0000-0002-8440-3362
Dominique Bouniol https://orcid.org/0000-0001-9020-1719
Florent Beucher https://orcid.org/0000-0002-1631-2450
Veronika Pörtge https://orcid.org/0000-0001-9019-6294
Michael Schäfer https://orcid.org/0000-0003-1896-1574
Alex Ayet https://orcid.org/0000-0002-4044-4488
Pierre-Etienne Brilouet https://orcid.org/0000-0002-1551-4966
Marek Jacob https://orcid.org/0000-0001-9059-6458
Martin Wirth https://orcid.org/0000-0001-5951-2252

REFERENCES

Atlas, D., Iguchi, T. and Pierce, H.F. (1995) Storm-induced wind patterns on the sea from spaceborne synthetic aperture radar. *Bulletin of the American Meteorological Society*, 76, 1585–1592.

Ayet, A., Rascle, N., Chapron, B., Couvreux, F. and Terray, L. (2021) Uncovering air-sea interaction in oceanic submesoscale frontal regions using high-resolution satellite observations. *US Clivar Variations*, 19, 10–17.

Barnes, H.C. and Houze, R.A. (2014) Precipitation hydrometeor type relative to the mesoscale airflow in mature oceanic deep convection of the Madden–Julian oscillation. *Journal of Geophysical Research: Atmospheres*, 119, 13–990.

Barthe, C., Asencio, N., Lafore, J.-P., Chong, M., Campistron, B. and Cazenave, F. (2010) Multi-scale analysis of the 25–27 July 2006 convective period over Niamey: Comparison between Doppler radar observations and simulations. *Quarterly Journal of the Royal Meteorological Society*, 136, 190–208.

Beucher, F., Couvreux, F., Bouniol, D., Faure, G., Favot, F., Dauhut, T. and Ayet, A. (2022) Process oriented evaluation of the oversea AROME configuration: Focus on the representation of cloud organisation. *Quarterly Journal of the Royal Meteorological Society*, 148(749), 3429–3447.

Bony, S. and Dufresne, J.-L. (2005) Marine boundary layer clouds at the heart of tropical cloud feedback uncertainties in climate models. *Geophysical Research Letters*, 32.

Bony, S., Schulz, H., Vial, J. and Stevens, B. (2020) Sugar, gravel, fish, and flowers: Dependence of mesoscale patterns of trade-wind clouds on environmental conditions. *Geophysical Research Letters*, 47, e2019GL085988.

Bony, S. and Stevens, B. (2019) Measuring area-averaged vertical motions with dropsondes. *Journal of the Atmospheric Sciences*, 76, 767–783.

Bony, S., Stevens, B., Ament, F., Bigorre, S., Chazette, P., Crewell, S., Delanoë, J., Emanuel, K., Farrell, D., Flamant, C., Gross, S., Hirsch, L., Karstensen, J., Mayer, B., Nuijens, L., Ruppert Jr., J.H., Sandu, I., Siebesma, P., Speich, S., Szczap, F., Totems, J., Vogel, R., Wendisch, M. and Wirth, M. (2017) EUREC^{4}A: A field campaign to elucidate the couplings between clouds, convection and circulation. *Surveys in Geophysics*, 38, 1529–1568.

Bretherton, C. and Blossey, P. (2017) Understanding mesoscale aggregation of shallow cumulus convection using Large-Eddy simulation. *Journal of Advances in Modeling Earth Systems*, 9, 2798–2821.

Brilouet, P.-E., Bouniol, D., Couvreux, F., Ayet, A., Granero-Belinchon, C., Lothon, M. and Mouche, A. (2022) Clear-sky turbulence and shallow convection: New insights combining SAR images and in situ measurements. *Geophysical Research Letters*. under review.

Cotton, W.R., Lin, M.-S., McAnelly, R.L. and Tremback, C.J. (1989) A composite model of mesoscale convective complexes. *Monthly Weather Review*, 117, 765–783.

Cuxart, J., Bougeault, P. and Redelsperger, J.-L. (2000) A turbulence scheme allowing for mesoscale and Large-Eddy simulations. *Quarterly Journal of the Royal Meteorological Society*, 126, 1–30.

Dauhut, T., Chaboureau, J.-P., Escobar, J. and Mascart, P. (2016) Giga-les of hector the convector and its two tallest updrafts up to the stratosphere. *Journal of the Atmospheric Sciences*, 73, 5041–5060.

Davini, P., D'Andrea, F., Park, S.-B. and Gentine, P. (2017) Coherent structures in Large-Eddy simulations of a nonprecipitating stratocumulus-topped boundary layer. *Journal of Atmospheric Sciences*, 74, 4117–4137.

Denby, L. (2020) Discovering the importance of mesoscale cloud organization through unsupervised classification. *Geophysical Research Letters*, 47, e2019GL085190.

Eastman, R., Warren, S.G. and Hahn, C.J. (2011) Variations in cloud cover and cloud types over the ocean from surface observations, 1954–2008. *Journal of Climate*, 24, 5914–5934.

Ewald, F., Kölling, T., Baumgartner, A., Zinner, T. and Mayer, B. (2016) Design and characterization of specmacs, a multipurpose hyperspectral cloud and sky imager. *Atmospheric Measurement Techniques*, 9, 2015–2042.

George, G., Stevens, B., Bony, S., Pincus, R., Fairall, C., Schulz, H., Kölling, T., Kalen, Q.T., Klingebiel, M., Konow, H., Lundry, A., Prange, M. and Radtke, J. (2021) JOANNE: Joint dropsonde observations of the atmosphere in tropical north atlantic meso-scale environments. *Earth System Science Data*, 13(11), 5253–5272.

Glenn, I.B. and Krueger, S.K. (2014) Downdrafts in the near cloud environment of deep convective updrafts. *Journal of Advances in Modeling Earth Systems*, 6, 1–8.

Gregory, D., Morcrette, J.-J., Jakob, C., Beljaars, A. and Stockdale, T. (2000) Revision of convection, radiation and cloud schemes in the ECMWF integrated forecasting system. *Quarterly Journal of the Royal Meteorological Society*, 126, 1685–1710.

Haerter, J.O., Böing, S.J., Henneberg, O. and Nissen, S.B. (2019) Circling in on convective organization. *Geophysical Research Letters*, 46, 7024–7034.

Houze, R.A. (1977) Structure and dynamics of a tropical squall–line system. *Monthly Weather Review*, 105, 1540–1567.

Houze, R.A. (2004) Mesoscale convective systems. *Reviews of Geophysics*, 42, R.

Houze, R.A., Jr., Cheng, C.-P., Leary, C.A. and Gamache, J.F. (1980) Diagnosis of cloud mass and heat fluxes from radar and synoptic data. *Journal of Atmospheric Sciences*, 37, 754–773.

Jacob, M., Ament, F., Gutleben, M., Konow, H., Mech, M., Wirth, M. and Crewell, S. (2019) Investigating the liquid water path over the tropical atlantic with synergistic airborne measurements. *Atmospheric Measurement Techniques*, 12, 3237–3254.

Khairoutdinov, M.F., Krueger, S.K., Moeng, C.-H., Bogenschutz, P.A. and Randall, D.A. (2009) Large-eddy Simulation Of Maritime Deep Tropical Convection. *Journal of Advances in Modeling Earth Systems*, 1, 15.

Kölling, T., Zinner, T. and Mayer, B. (2019) Aircraft-based stereographic reconstruction of 3-d cloud geometry. *Atmospheric Measurement Techniques*, 12, 1155–1166.

Konow, H., Ewald, F., George, G., Jacob, M., Klingebiel, M., Kölling, T., Luebke, A.E., Mieslinger, T., Pörtge, V., Radtke, J., Schäfer, M., Schulz, H., Vogel, R., Wirth, M., Bony, S., Crewell, S., Ehrlich, A., Forster, L., Giez, A., Gödde, F., Groß, S., Gutleben, M., Hagen, M., Hirsch, L., Jansen, F., Lang, T., Mayer, B., Mech, M., Prange, M., Schnitt, S., Vial, J., Walbröl, A., Wendisch, M., Wolf, K., Zinner, T., Zöger, M., Ament, F. and Stevens, B. (2021) EUREC^4 A's HALO. *Earth System Science Data*, 13, 5545–5563.

Lac, C., Chaboureau, J.-P., Masson, V., Pinty, J.-P., Tulet, P., Escobar, J., Leriche, M., Barthe, C., Aouizerats, B., Augros, C., Aumond, P., Auguste, F., Bechtold, P., Berthet, S., Bielli, S., Bosseur, F., Caumont, O., Cohard, J.-M., Colin, J., Couvreux, F., Cuxart, J., Delautier, G., Dauhut, T., Ducrocq, V., Filippi, J.-B., Gazen, D., Geoffroy, O., Gheusi, F., Honnert, R., Lafore, J.-P., Lebeaupin Brossier, C., Libois, Q., Lunet, T., Mari, C., Maric, T., Mascart, P., Mogé, M., Molinié, G., Nuissier, O., Pantillon, F., Peyrillé, P., Pergaud, J., Perraud, E., Pianezze, J., Redelsperger, J.-L., Ricard, D., Richard, E., Riette, S., Rodier, Q., Schoetter, R., Seyfried, L., Stein, J., Suhre, K., Taufour, M., Thouron, O., Turner, S., Verrelle, A., Vié, B., Visentin, F., Vionnet, V. and Wautelet, P. (2018) Overview of the Meso-NH model version 5.4 and its applications. *Geoscientific Model Development*, 11, 1929–1969.

LeMone, M.A. (1983) Momentum transport by a line of cumulonimbus. *Journal of Atmospheric Sciences*, 40, 1815–1834.

LeMone, M.A. and Pennell, W.T. (1976) The relationship of trade wind cumulus distribution to subcloud layer fluxes and structure. *Monthly Weather Review*, 104, 524–539.

LeMone, M.A., Barnes, G.M., Szoke, E.J. and Zipser, E.J. (1984) The tilt of the leading edge of mesoscale tropical convective lines. *Monthly weather review*, 112(3), 510–519.

Mech, M., Orlandi, E., Crewell, S., Ament, F., Hirsch, L., Hagen, M., Peters, G. and Stevens, B. (2014) HAMP–the microwave package on the high altitude and long range research aircraft (HALO). *Atmospheric Measurement Techniques*, 7, 4539–4553.

Meyer, B. and Haerter, J.O. (2020) Mechanical forcing of convection by cold pools: Collisions and energy scaling. *Journal of Advances in Modeling Earth Systems*, 12, e2020MS002281.

Narenpitak, P., Kazil, J., Yamaguchi, T., Quinn, P.K. and Feingold, G. (2021) From sugar to flowers: A transition of shallow cumulus organization during ATOMIC. *Journal of Advances in Modeling Earth Systems*, 13, e2021MS002619.

Naumann, A.K., Stevens, B., Hohenegger, C. and Mellado, J.P. (2017) A conceptual model of a shallow circulation induced by prescribed low-level radiative cooling. *Journal of the Atmospheric Sciences*, 74, 3129–3144.

Nicholls, S. and Lemone, M.A. (1980) The fair weather boundary layer in GATE: The relationship of subcloud fluxes and structure to the distribution and enhancement of cumulus clouds. *Journal of Atmospheric Sciences*, 37, 2051–2067.

Pinty, J.-P. and Jabouille, P. (1998) A mixed-phase cloud parameterization for use in mesoscale nonhydrostatic model: Simulations of a squall line and of orographic precipitations., In: *Proceedings of the Conference on Cloud Physics, 217–220*. Amer. Meteor, Soc Everett, WA.

Qu, X., Hall, A., Klein, S.A. and Caldwell, P.M. (2015) The strength of the tropical inversion and its response to climate change in 18 CMPI5 models. *Climate Dynamics*, 45, 375–396.

Rasp, S., Schulz, H., Bony, S. and Stevens, B. (2020) Combining crowdsourcing and deep learning to explore the mesoscale organization of shallow convection. *Bulletin of the American Meteorological Society*, 101, E1980–E1995.

Rochetin, N., Hohenegger, C., Touzé-Peiffer, L. and Villefranque, N. (2021) A physically based definition of convectively generated density currents: Detection and characterization in convection-permitting simulations. *Journal of Advances in Modeling Earth Systems*, 13, e2020MS002402.

Rodts, S.M., Duynkerke, P.G. and Jonker, H.J. (2003) Size distributions and dynamical properties of shallow cumulus clouds from aircraft observations and satellite data. *Journal of the Atmospheric Sciences*, 60, 1895–1912.

Rotunno, R., Klemp, J.B. and Weisman, M.L. (1988) A theory for strong, long-lived squall lines. *Journal of Atmospheric Sciences*, 45, 463–485.

Schäfer, M., Wolf, K., Ehrlich, A., Hallbauer, C., Jäkel, E., Jansen, F., Luebke, A.E., Müller, J., Thoböll, J., Röschenthaler, T., Stevens, B. and Wendisch, M. (2021) VELOX—A new thermal infrared imager for airborne remote sensing of cloud and surface properties. *Atmospheric Measurement Techniques*, 15, 1491–1509.

Schlemmer, L. and Hohenegger, C. (2014) The formation of wider and deeper clouds as a result of cold-pool dynamics. *Journal of the Atmospheric Sciences*, 71, 2842–2858.

Schulz, H., Eastman, R. and Stevens, B. (2021) Characterization and evolution of organized shallow convection in the downstream

1477870x, 2023, 750, Downloaded from https://rmets.onlinelibrary.wiley.com/doi/10.1002/qj.4409 by Portail BibCNRS INS2I, Wiley Online Library on [25/10/2023]. See the Terms and Conditions (https://onlinelibrary.wiley.com/terms-and-conditions) on Wiley Online Library for rules of use; OA articles are governed by the applicable Creative Commons License

north atlantic trades. *Journal of Geophysical Research: Atmospheres*, 126, e2021JD034575.

Stevens, B., Bony, S., Brogniez, H., Hentgen, L., Hohenegger, C., Kiemle, C., L'Ecuyer, T.S., Naumann, A.K., Schulz, H., Siebesma, P.A., Vial, J., Winker, D.M. and Zuidema, P. (2020) Sugar, gravel, fish and flowers: Mesoscale cloud patterns in the trade winds. *Quarterly Journal of the Royal Meteorological Society*, 146, 141–152.

Stevens, B., Bony, S., Farrell, D., Ament, F., Blyth, A., Fairall, C., Karstensen, J., Quinn, P.K., Speich, S., Acquistapace, C., Aemisegger, F., Albright, A.L., Bellenger, H., Bodenschatz, E., Caesar, K.-A., Chewitt-Lucas, R., de Boer, G., Delanoë, J., Denby, L., Ewald, F., Fildier, B., Forde, M., George, G., Gross, S., Hagen, M., Hausold, A., Heywood, K.J., Hirsch, L., Jacob, M., Jansen, F., Kinne, S., Klocke, D., Kölling, T., Konow, H., Lothon, M., Mohr, W., Naumann, A.K., Nuijens, L., Olivier, L., Pincus, R., Pöhlker, M., Reverdin, G., Roberts, G., Schnitt, S., Schulz, H., Siebesma, A.P., Stephan, C.C., Sullivan, P., Touzé-Peiffer, L., Vial, J., Vogel, R., Zuidema, P., Alexander, N., Alves, L., Arixi, S., Asmath, H., Bagheri, G., Baier, K., Bailey, A., Baranowski, D., Baron, A., Barrau, S., Barrett, P.A., Batier, F., Behrendt, A., Bendinger, A., Beucher, F., Bigorre, S., Blades, E., Blossey, P., Bock, O., Böing, S., Bosser, P., Bourras, D., Bouruet-Aubertot, P., Bower, K., Branellec, P., Branger, H., Brennek, M., Brewer, A., Brilouet, P.-E., Brügmann, B., Buehler, S.A., Burke, E., Burton, R., Calmer, R., Canonici, J.-C., Carton, X., Cato Jr., G., Charles, J.A., Chazette, P., Chen, Y., Chilinski, M.T., Choularton, T., Chuang, P., Clarke, S., Coe, H., Cornet, C., Coutris, P., Couvreux, F., Crewell, S., Cronin, T., Cui, Z., Cuypers, Y., Daley, A., Damerell, G.M., Dauhut, T., Deneke, H., Desbios, J.-P., Dörner, S., Donner, S., Douet, V., Drushka, K., Dütsch, M., Ehrlich, A., Emanuel, K., Emmanouilidis, A., Etienne, J.-C., Etienne-Leblanc, S., Faure, G., Feingold, G., Ferrero, L., Fix, A., Flamant, C., Flatau, P.J., Foltz, G.R., Forster, L., Furtuna, I., Gadian, A., Galewsky, J., Gallagher, M., Gallimore, P., Gaston, C., Gentemann, C., Geyskens, N., Giez, A., Gollop, J., Gouirand, I., Gourbeyre, C., de Graaf, D., de Groot, G.E., Grosz, R., Güttler, J., Gutleben, M., Hall, K., Harris, G., Helfer, K.C., Henze, D., Herbert, C., Holanda, B., Ibanez-Landeta, A., Intrieri, J., Iyer, S., Julien, F., Kalesse, H., Kazil, J., Kellman, A., Kidane, A.T., Kirchner, U., Klingebiel, M., Körner, M., Kremper, L.A., Kretzschmar, J., Krüger, O., Kumala, W., Kurz, A., L'Hégaret, P., Labaste, M., Lachlan-Cope, T., Laing, A., Landschützer, P., Lang, T., Lange, D., Lange, I., Laplace, C., Lavik, G., Laxenaire, R., Le Bihan, C., Leandro, M., Lefevre, N., Lena, M., Lenschow, D., Li, Q., Lloyd, G., Los, S., Losi, N., Lovell, O., Luneau, C., Makuch, P., Malinowski, S., Manta, G., Marinou, E., Marsden, N., Masson, S., Maury, N., Mayer, B., Mayers-Als, M., Mazel, C., McGeary, W., McWilliams, J.C., Mech, M., Mehlmann, M., Meroni, A.N., Mieslinger, T., Minikin, A., Minnett, P., Möller, G., Morfa Avalos, Y., Muller, C., Musat, I., Napoli, A., Neuberger, A., Noisel, C., Noone, D., Nordsiek, F., Nowak, J.L., Oswald, L., Parker, D.J., Peck, C., Person, R., Philippi, M., Plueddemann, A., Pöhlker, C., Pörtge, V., Pöschl, U., Pologne, L., Posyniak, M., Prange, M., Quiñones Meléndez, E., Radtke, J., Ramage, K., Reimann, J., Renault, L., Reus, K., Reyes, A., Ribbe, J., Ringel, M., Ritschel, M., Rocha, C.B., Rochetin, N., Röttenbacher, J., Rollo, C., Royer, H., Sadoulet, P., Saffin, L., Sandiford, S., Sandu, I., Schäfer, M., Schemann, V., Schirmacher, I., Schlenczek, O., Schmidt, J., Schröder, M., Schwarzenboeck, A., Sealy, A., Senff, C.J., Serikov, I., Shohan, S., Siddle, E., Smirnov, A., Späth, F., Spooner, B., Stolla, M.K., Szkółka, W., de Szoeke, S.P., Tarot, S., Tetoni, E., Thompson, E., Thomson, J., Tomassini, L., Totems, J., Ubele, A.A., Villiger, L., von Arx, J., Wagner, T., Walther, A., Webber, B., Wendisch, M., Whitehall, S., Wiltshire, A., Wing, A.A., Wirth, M., Wiskandt, J., Wolf, K., Worbes, L., Wright, E., Wulfmeyer, V., Young, S., Zhang, C., Zhang, D., Ziemen, F., Zinner, T. and Zöger, M. (2021) EUREC^{4}A. *Earth System Science Data*, 13, 4067–4119.

Strauss, C., Ricard, D. and Lac, C. (2021) Dynamics of the cloud-environment interface and turbulence effects in a LES of a growing cumulus congestus. *Journal of the Atmospheric Sciences*, 15, 1491–1509.

Touzé-Peiffer, L., Vogel, R. and Rochetin, N. (2022). Cold Pools Observed during EUREC4A: Detection and Characterization from Atmospheric Soundings. *Journal of Applied Meteorology and Climatology*, 61(5), 593–610.

Wilson, J.W. and Schreiber, W.E. (1986) Initiation of convective storms at radar-observed boundary-layer convergence lines. *Monthly Weather Review*, 114, 2516–2536.

Wirth, M., Fix, A., Mahnke, P., Schwarzer, H., Schrandt, F. and Ehret, G. (2009) The airborne multi-wavelength water vapor differential absorption lidar wales: System design and performance. *Applied Physics B*, 96, 201–213.

Wood, R. and Bretherton, C.S. (2006) On the relationship between stratiform low cloud cover and lower-tropospheric stability. *Journal of Climate*, 19, 6425–6432.

Young, G.S., Sikora, T.D. and Winstead, N.S. (2000) Inferring marine atmospheric boundary layer properties from spectral characteristics of satellite-borne SAR imagery. *Monthly Weather Review*, 128, 1506–1520.

Zipser, E. (1977) Mesoscale and convective–scale downdrafts as distinct components of squall-line structure. *Monthly Weather Review*, 105, 1568–1589.

Zuidema, P., Li, Z., Hill, R.J., Bariteau, L., Rilling, B., Fairall, C., Brewer, W.A., Albrecht, B. and Hare, J. (2012) On trade wind cumulus cold pools. *Journal of the Atmospheric Sciences*, 69, 258–280.

SUPPORTING INFORMATION

Additional supporting information can be found online in the Supporting Information section at the end of this article.

How to cite this article: Dauhut, T., Couvreux, F., Bouniol, D., Beucher, F., Volkmer, L., Pörtge, V. *et al.* (2023) Flower trade-wind clouds are shallow mesoscale convective systems. *Quarterly Journal of the Royal Meteorological Society*, 149(750), 325–347. Available from: https://doi.org/10.1002/qj.4409

1477870x, 2023, 750, Downloaded from https://rmets.onlinelibrary.wiley.com/doi/10.1002/qj.4409 by Portail BibCNRS INSU, Wiley Online Library on [25/10/2023]. See the Terms and Conditions (https://onlinelibrary.wiley.com/terms-and-conditions) on Wiley Online Library for rules of use; OA articles are governed by the applicable Creative Commons License